

Supplementary Information

Room-temperature logic-in-memory operations in single-metallofullerene devices

Jing Li,^{1,4} Songjun Hou,^{2,4} Yang-Rong Yao,^{1,4} Chengyang Zhang,^{1,4} Qingqing Wu,² Hai-Chuan Wang,¹ He-Wei Zhang,¹ Xinyuan Liu,¹ Chun Tang,¹ Mengxi Wei,¹ Wei Xu,¹ Yaping Wang,¹ Jueting Zheng,¹ Zhichao Pan,¹ Lixing Kang,³ Junyang Liu,¹ Jia Shi,¹ Yang Yang,¹ Colin Lambert,^{2*} Su-Yuan Xie,^{1*} Wenjing Hong^{1*}

¹State Key Laboratory of Physical Chemistry of Solid Surfaces, College of Chemistry and Chemical Engineering & IKKEM, Xiamen University, Xiamen, 361005, P. R. China.

²Department of Physics, Lancaster University, Lancaster LA 14 YB, United Kingdom

³Key Laboratory of Multifunctional Nanomaterials and Smart Systems, Division of Advanced Materials, Suzhou Institute of Nano-Tech and Nano-Bionics, Chinese Academy of Sciences, Suzhou 215123, China

⁴These authors contributed equally: Jing Li, Songjun Hou, Yang-Rong Yao, Chengyang Zhang

Correspondence to: c.lambert@lancaster.ac.uk, syxie@xmu.edu.cn, and whong@xmu.edu.cn

Table of Contents

S1. Single-spin bistability and single permanent polarized electrical dipole bistability

S2. Discussion on the scalability of the single-metallofullerene device

S3. Conductance-voltage measurements

S4. The *in-situ* bias voltage controlled two-conductance-state switching and storage operation

S5. The experiments using mechanically controllable break junction (MCBJ) technique

S6. The *in-situ* logic-in-memory operations

S7. Theoretical Calculation and Simulation

S8. Molecular preparation and chemical nomenclature

S1. Single-spin bistability and single permanent polarized electrical dipole bistability

Spin and electrical dipole play pivotal roles in the current computing and information technology, such as hard disk, ferroelectric devices. The fundamentals of devices are settled by the magnetic random access memories (MRAMs) or ferroelectric random access memories (FeRAMs), and both of them have their characteristics. With the relentless minimization of integrated circuit size to nanoscale or single-molecule, this situation changes from the theoretical point of view.¹ Recall the Heisenberg model of the two bulk materials (ferromagnet and ferroelectric), both of them are composed of coupling interaction between the spin or electrical dipole, and anisotropy of single spin or electrical dipole: $H = -J \sum_{\langle i,j \rangle} \sigma_i \sigma_j - D \sum_j (\sigma_{jz})^2$

in which J represents the magnitude of exchange coupling between the spin or electrical dipole, D represents the anisotropy energy of the spin or electrical dipole.

For the spin system, the magnitude of exchange coupling J and the spin anisotropy D is smaller than 10 meV. Hence, the energy cost for spin flipping in MRAMs is $NJ + D$, which depends mostly on the number of adjacent spin centers. For the nanoscale material or single-molecule, the number of adjacent spins N is reduced, so the energy cost for spin flipping is reduced. So far, the blocking temperature of most single-molecule magnets is in the liquid helium temperature region.

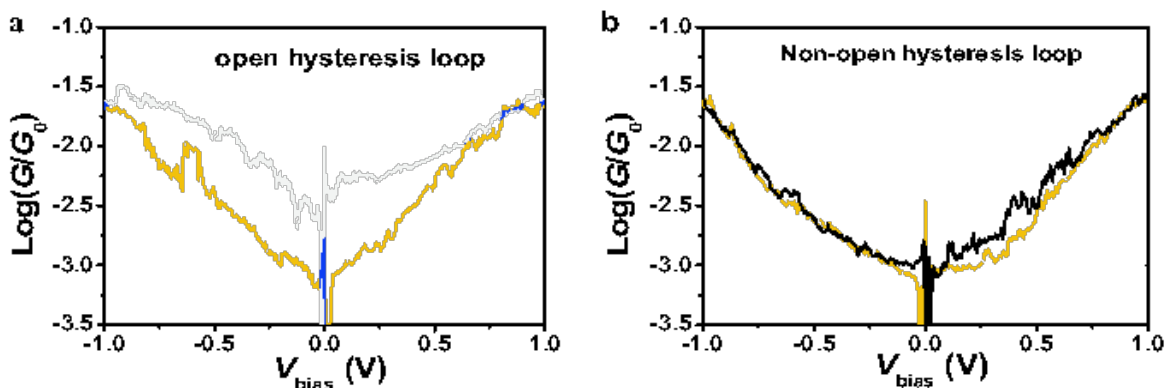
For the electrical dipole system, the magnitude of exchange coupling J and the spin anisotropy D can reach hundreds of meV by tuning the chemical bond. As a result, the Curie temperature of ferroelectric materials is usually higher than room temperature. When the number of adjacent dipoles is reduced, even for a single electric dipole, a high Curie temperature can still be maintained. But until now, no experimental results proved it at the single-molecule scale.

In theory, it is hard to realize non-volatile memory devices by operating spin-flip at the single-molecule scale at room temperature, but it may be possible to achieve by manipulating the flip of a single electric dipole.

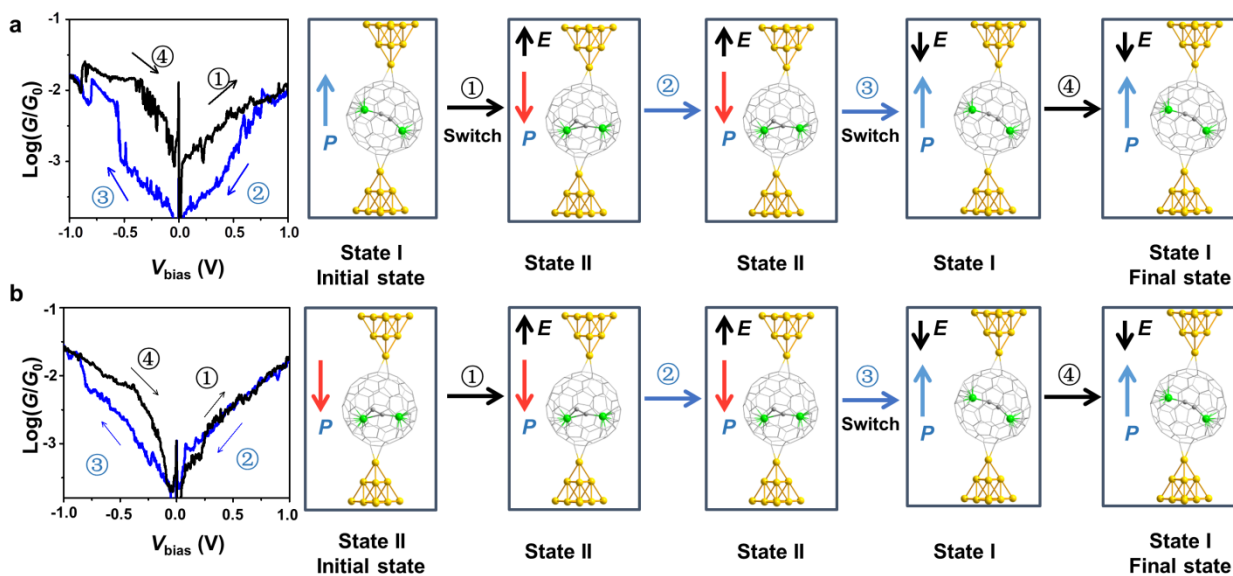
S2. Discussion on the scalability of the single-metallofullerene device

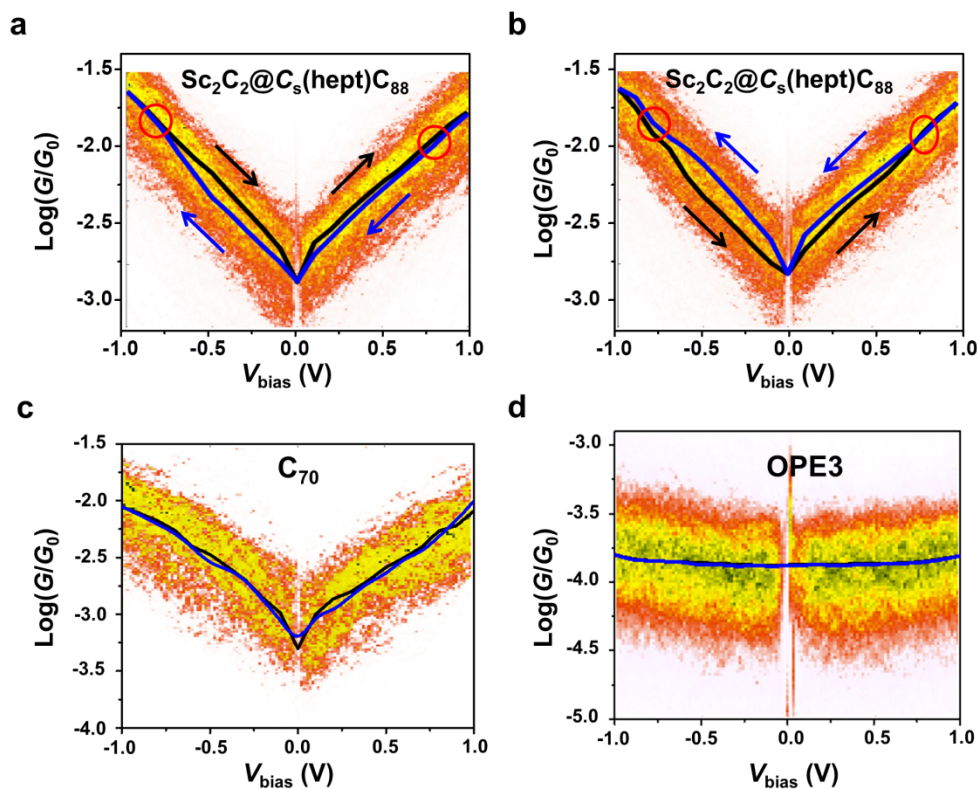
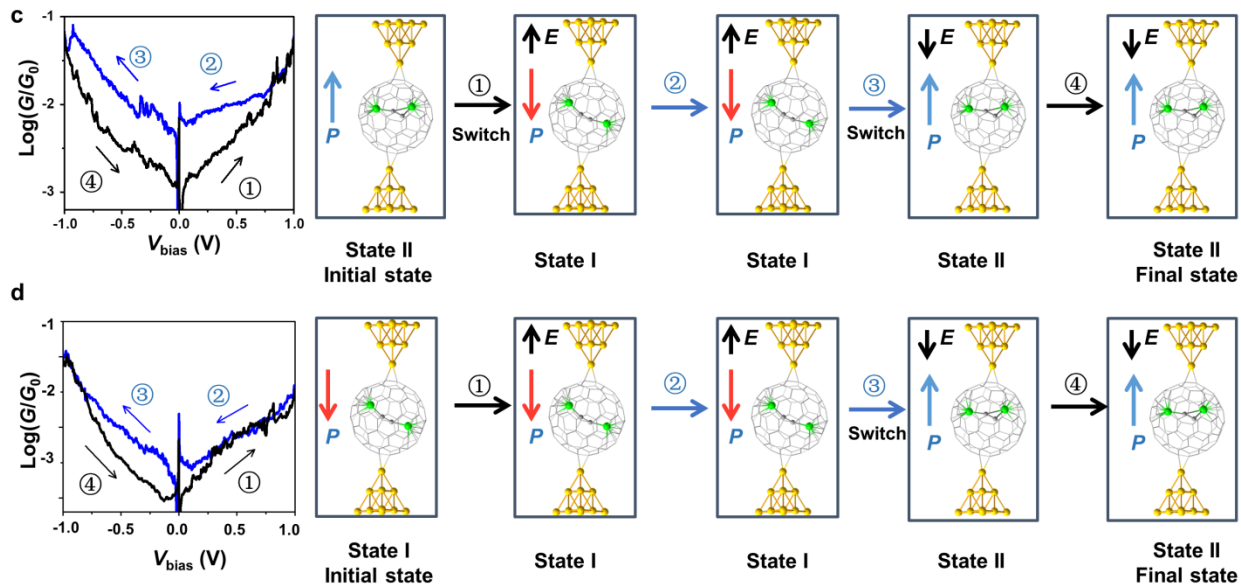
In conventional CMOS devices, the channel length is one of the key factors affecting the performance of a device, such as operation voltage, subthreshold swing, leakage current, and energy consumption. Scientists are pursuing short channels to achieve high performance of the chip. In a single-molecule device, the size of the molecule is similar to the channel length in a CMOS device. For the scalability, our single-metallofullerene device is about 1.5 nm^2 in size according to the diameter of our metallofullerene molecule, which is theoretically the ultimate solution for high-density integration and low-power manipulation. Similar to a silicon-based CMOS device, external electrodes as connections are needed, which would make the size of the device larger to be $5\sim 10 \text{ nm}^2$.²

S3. Conductance-voltage measurements

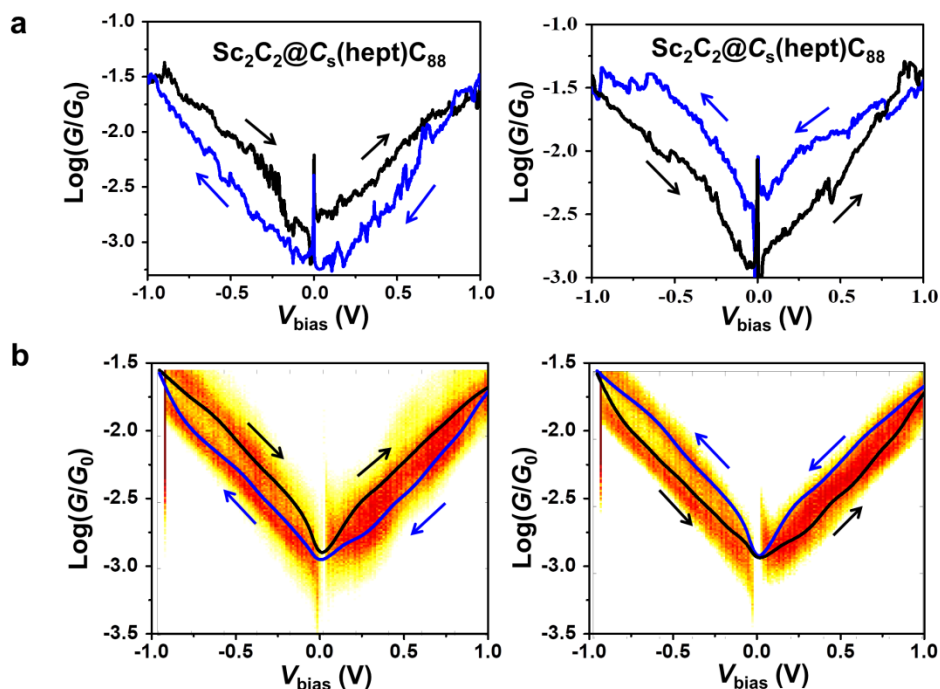


Supplementary Fig. 1| The typical G - V curves. **a**, Open hysteresis loop. **b**, Non-open hysteresis loop. Approximately 81% (941 in 1162) of curves showed the loops according to the statistical analysis. The main reason for non-open hysteresis loop could be that if the dipole component of the initial configuration of the molecular junctions in the direction of the current flow coupled with the electric field under the infinite bias voltage cannot reach the threshold energy barrier, no open hysteresis loop can be observed within the applied bias voltages.



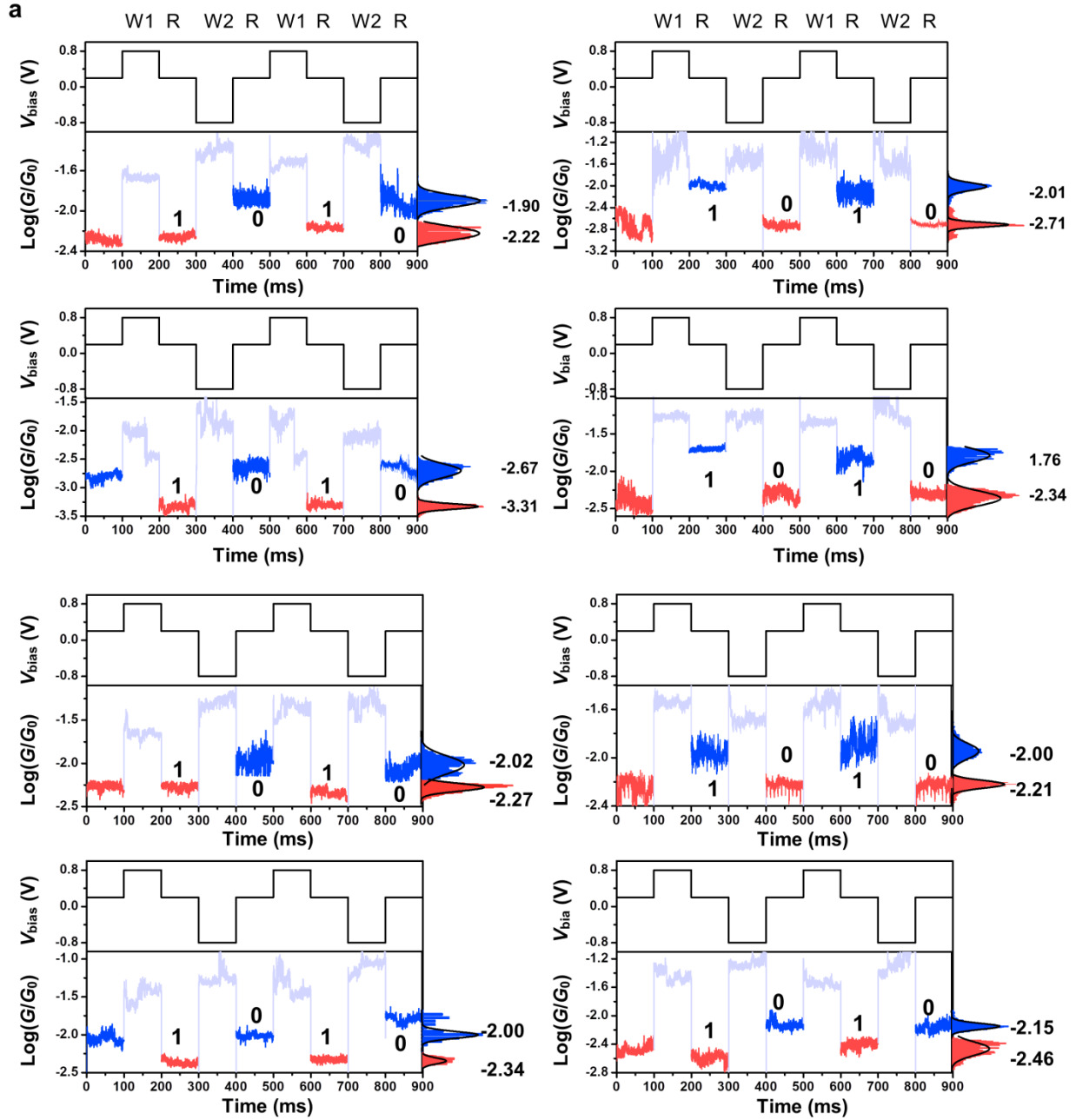


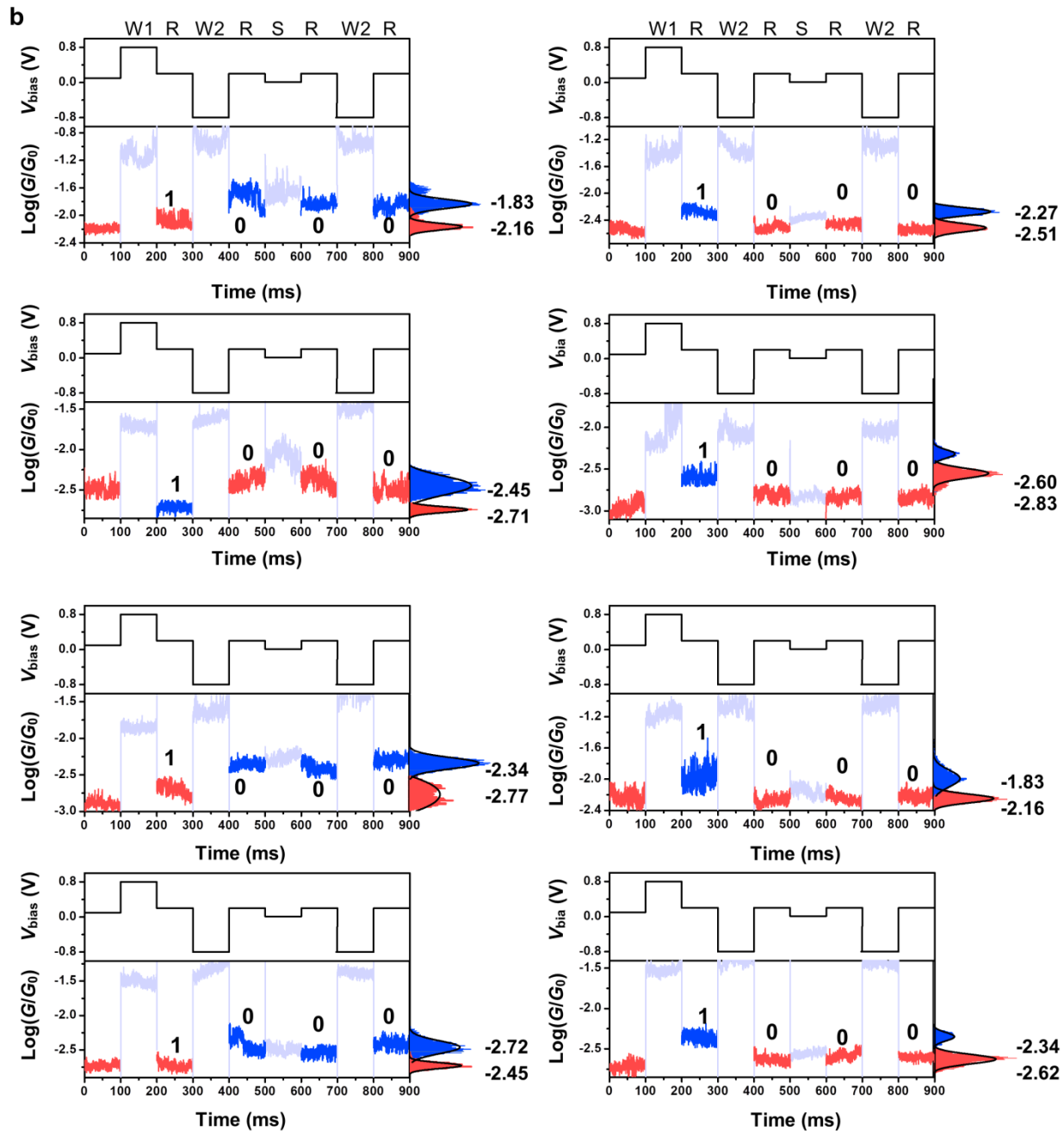
respectively. The solid lines are the statistical G - V curves. The arrows represent the bias voltages sweep directions. The open-loop is closed at the bias voltage around ± 0.7 V (marked by red circle), indicating a statistical threshold bias voltage ~ 0.7 V. It should be noted that the open-loop in the positive applied voltage range is much smaller than the one in the negative range. This phenomenon can be attributed to the fact that numbers of randomly formed devices did not switch their molecular state in the positive voltage range. **c-d**, G - V curves of C_{70} and 1,4-bis((4-(methylthio)phenyl)ethynyl)benzene (OPE3) as control experiments. No open electric hysteresis loops were observed in both samples. The color code represents the relative occurrence of G - V data points within the initial data sets in these density plots.



Supplementary Fig. 4 | The typical single G - V curves and the related statistical G - V curves of endohedral metallofullerenes $Sc_2C_2@Cs(hept)-C_{88}$ measured in a dry state in a nitrogen-protected glove box. **a**, The typical single G - V curves. **b**, The related statistical G - V curves.

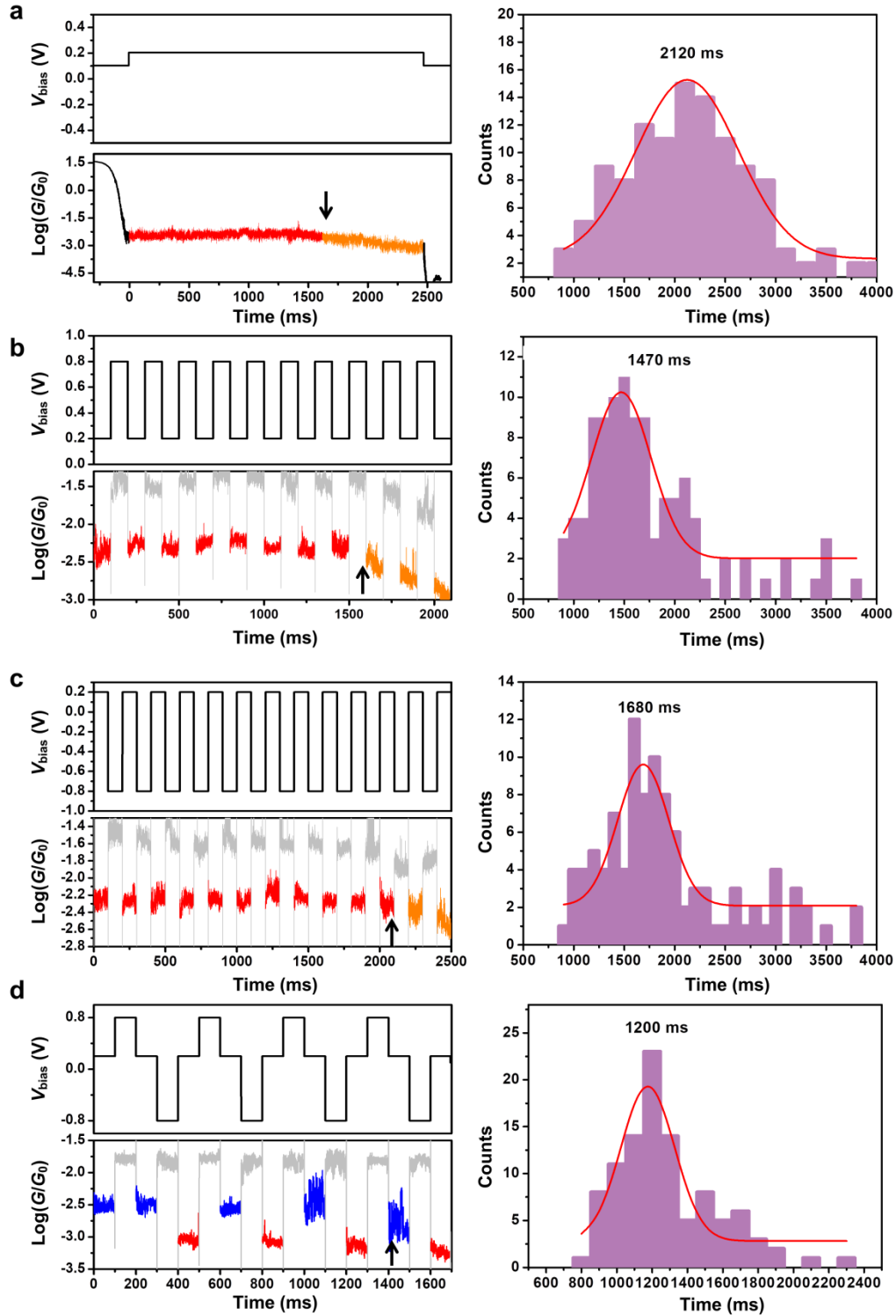
S4. The *in-situ* bias voltage controlled two-conductance-state switching and storage operation





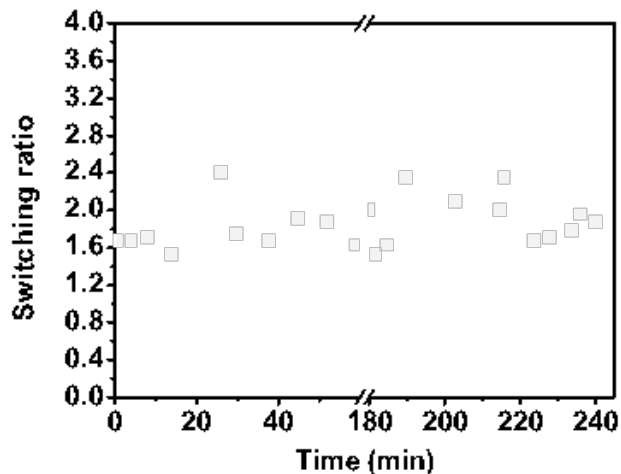
Supplementary Fig. 5 | Demonstration of the typical *in-situ* two-conductance-state switching and storage operation in single-metallofullerene devices of $\text{Sc}_2\text{C}_2@ \text{Cs}(\text{hept})\text{-C}_{88}$. **a**, Eight devices exhibit *in-situ* “two-conductance-state switching” operations. **b**, Eight devices exhibit non-volatile memory characteristics. In the experiments, +0.8 V (marked as W₁) is used to write the ‘1’ state, -0.8 V (marked as W₀) to write the ‘0’ state, and +0.2 V (marked as R) to read out the digital information through the conductance of the molecule, respectively. To ensure data collection, we treated +0.01 V as 0 (marked as S) to exhibit the non-volatile memory characteristics. The switching ratio between the high conductance state and the low conductance state

are between 150% and 500%.

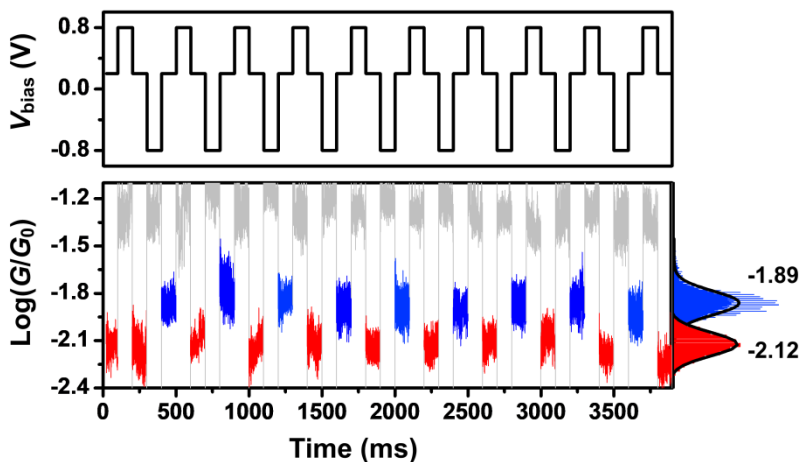


Supplementary Fig. 6| The molecular junction lifetime under different voltage pulses. a, The absence of pulses. **b**, Positive pulses (0.8 V) are applied repeatedly. **c**, Negative pulses (0.8 V) are applied repeatedly. **d**,

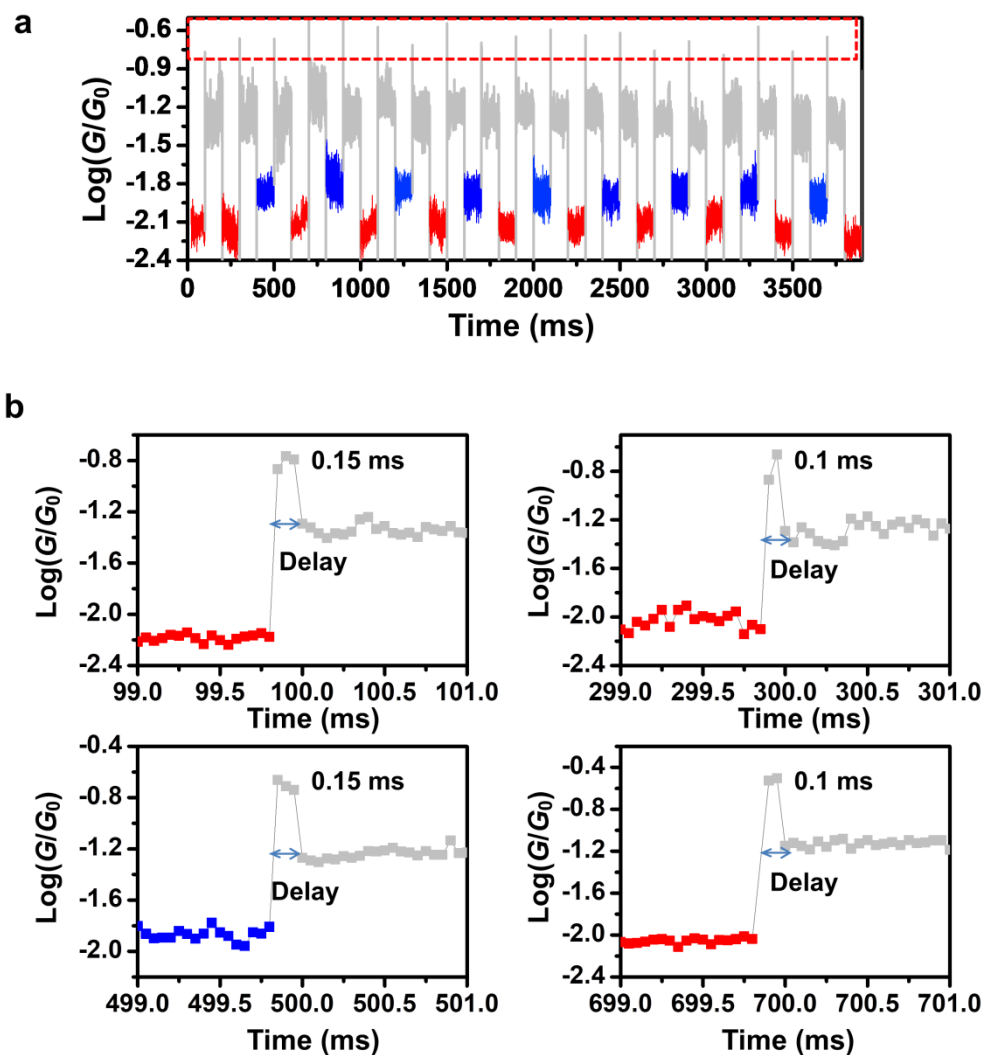
Pulses are applied by opposing signs to toggle the switch back and forth. The black arrow indicates that the molecular junction has drifted. For each set of experiments, more than 100 junctions are counted. By comparing the junction lifetime under different voltage pulses, the drift stability of the tip positioning is the possible reason to limit the junction lifetime, which is the typical characteristic of STM equipment.



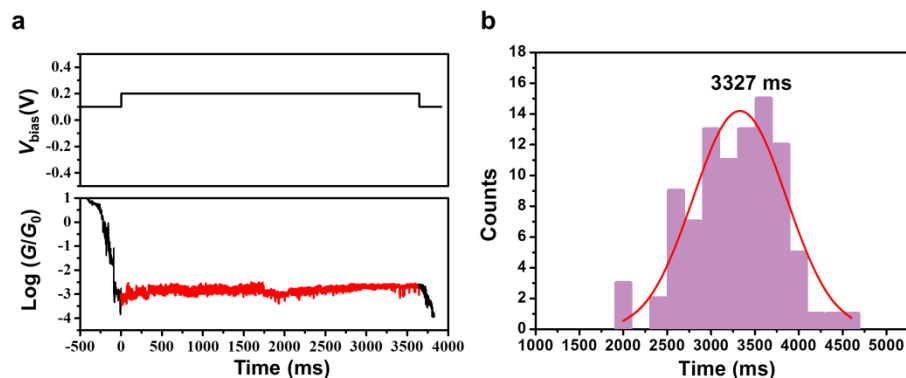
Supplementary Fig.7| The switching ratio (C_{HCS}/C_{LCS}) versus time of two-conductance-state switching molecular junctions with lifetime longer than 900 ms during a four-hour experiment.



Supplementary Fig.8| One junction showed a lifetime of 3900 ms and 19 switching cycles without degradation under a voltage pulse toggling the switch back and forth.



Supplementary Fig. 9] The transformation time related to the motion of the $[\text{Sc}_2\text{C}_2]$ cluster in a single-metallofullerene junction shown in Supplementary Fig. 8. a, Real-time current trace of a single-metallofullerene device. Voltage pulses of ± 0.8 V is applied for 100 ms and the transition state signal is observed during the initial of the switching voltage pulse (red dot rectangle). b, Magnified view of the four segments in the entire current trace. The transformation time is 0.1~ 0.15 ms.



Supplementary Fig. 10| The molecular junction lifetime of C₇₀. **a**, The typical junction of C₇₀. **b**, The typical lifetime of a single-C₇₀ junction

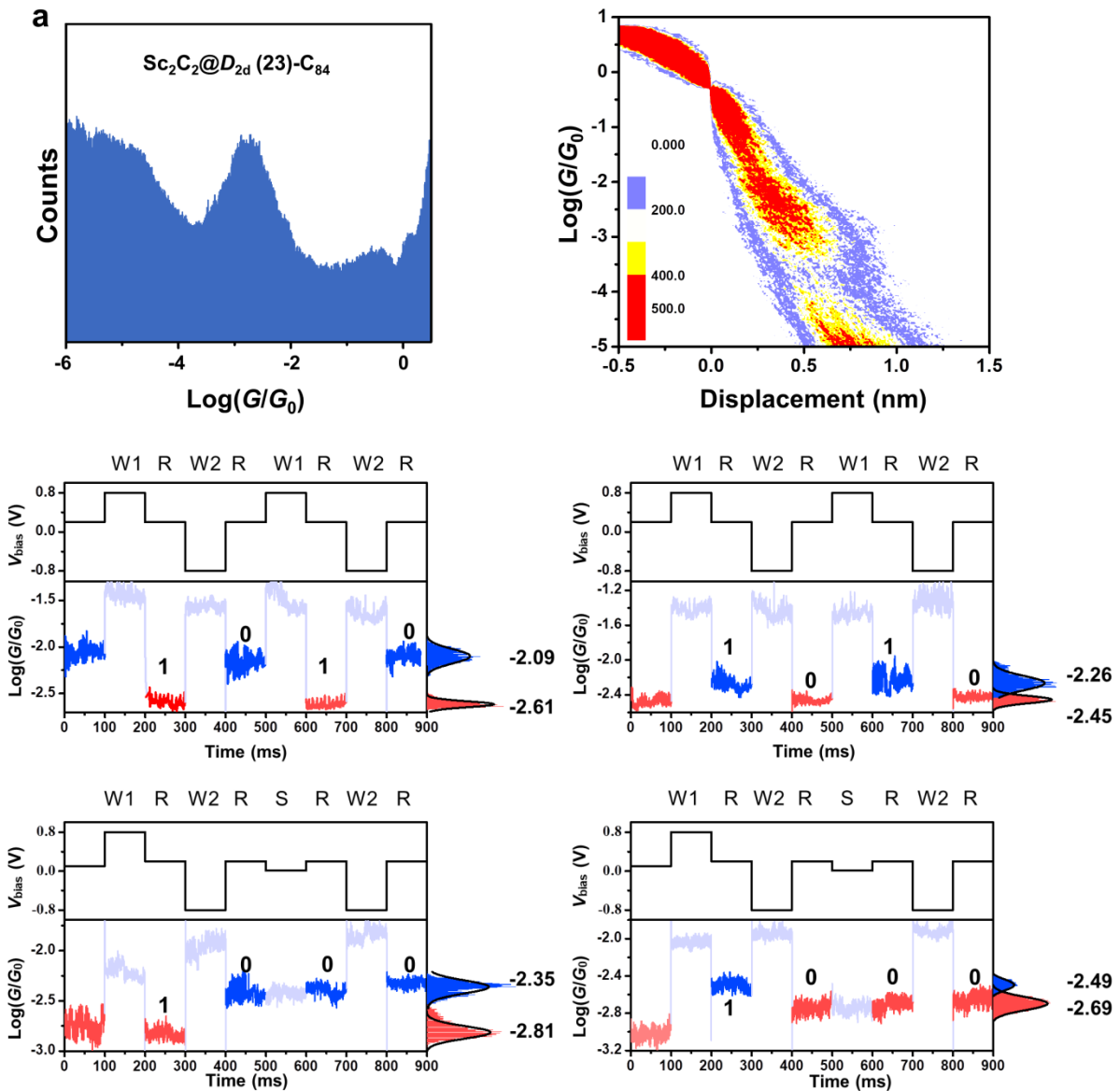
To further evaluate the stability and reproducibility of the single-fullerene junction, we studied the lifetime of the junctions from more than 100 junctions that are measured with different voltage pulses. We found that the typical lifetime of single-molecule junctions in our STMBJ setup is ~2120 ms. The lifetime of the junctions becomes shorter than the absence of the voltage pulses due to the drifting of the STM tip from the local heating effect (~1200 ms vs. 2100 ms), but still within the same order of magnitude (**Supplementary Fig. 6**).

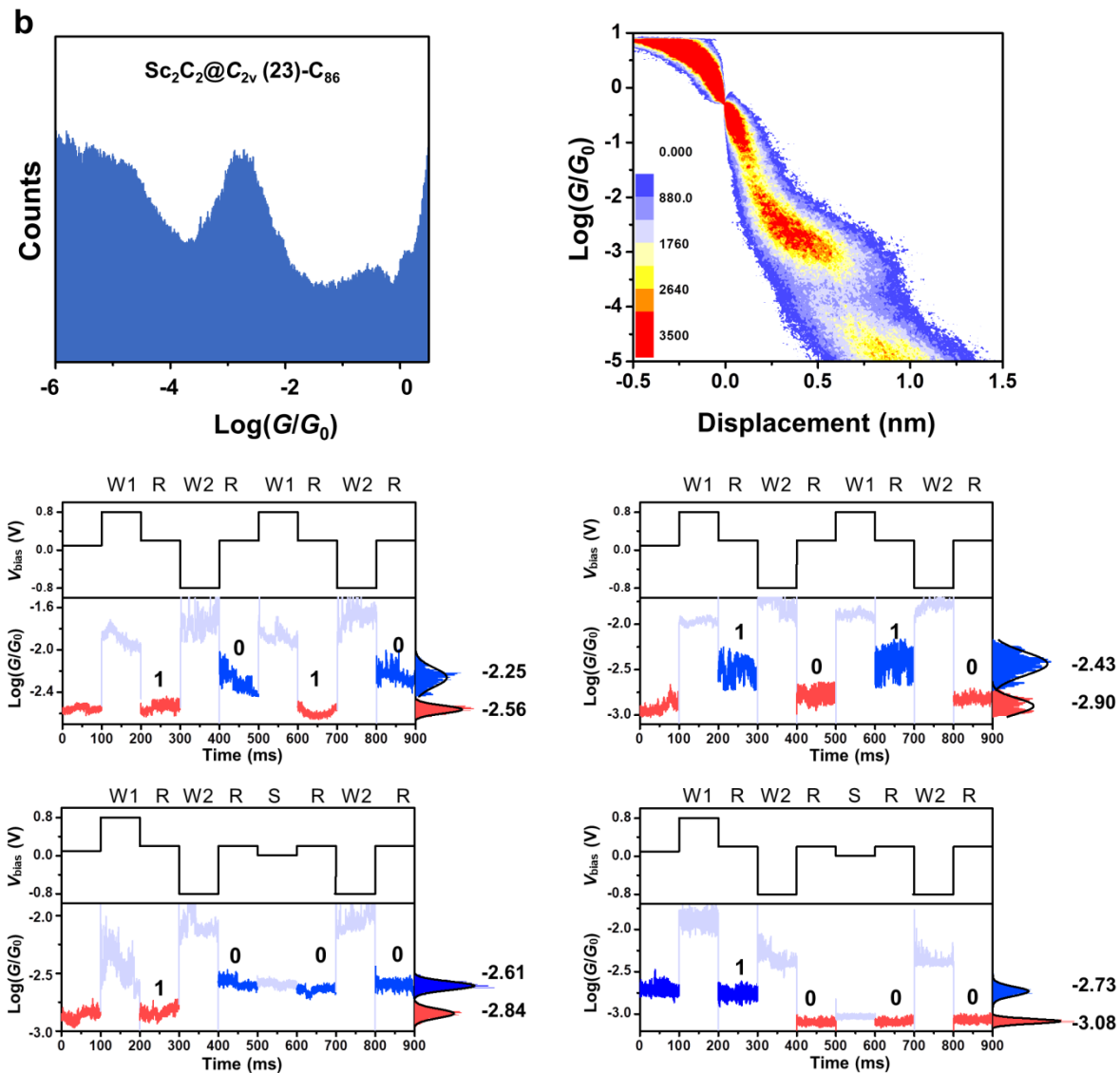
To further evaluate the degradation over time, we counted 46 two-conductance-state switching molecular junctions with lifetime longer than 900 ms during a four-hour experiment (**Supplementary Fig.7**), which have no obvious degradation of the switching ratio (~1.5-2.4) before the junction breakdown. To evaluate the possible degradation in the single-molecule junctions, our experiment also shows 19 switching cycles without degradation (**Supplementary Fig.8**), suggesting the stability and reproducibility of the electric-field induced bipolar conductance switches. Principally, the Sc₂C₂@Cs(hept)-C₈₈ molecule is stable and has been maintained for more than four years under atmospheric conditions without degradation, ensuring that the device is not affected by the stability of the molecule.

The switching time of the junction is a crucial parameter for its applications. According to the single-molecule switching reported by Miyamachi *et al.*,³ the transformation process can be detected by a high conductance delay during the initialization of the switching voltage pulse if the circuit response rate is faster than the polarization rate. In our experiments, the majority of junctions did not show a high conductance delay process in the current trace, indicating the transformation time related to the motion of the [Sc₂C₂] cluster is less than 0.05 ms. The short transformation time is reasonable because the reorientation of the [Sc₂C₂] cluster belongs to orientational polarization and atomic polarization, and its theoretical transition time could be in 10⁻⁵~10⁻¹² s range.⁴ In minority junctions, the high conductance delay is observed in the current trace when a high voltage pulse is applied. The longer switching time may be that the molecule undergoes multiple transition state during the transformation processes. We selected a 3.9 s lifetime junction as an example (**Supplementary Fig. 8**) to provide a more detailed analysis. A relatively high conductance peak was observed following the addition of a

switching voltage pulse, followed by a rapid small decrease (red dot rectangle in **Supplementary Fig. 9a**). As shown in **Supplementary Fig. 9b**, the time of the high conductance delay is approximately 0.1~0.15 ms.

The junction lifetime of C_{70} as a non-polar control molecule is also studied at the same condition (**Supplementary Fig.10**). The lifetime for the single- C_{70} junctions with a maximum probability of about ~3327 ms, which is slightly longer than that of the polar $Sc_2C_2@Cs(\text{hept})-C_{88}$ molecule, but still within the same order of magnitude, indicating that electrical dipolar character of the molecule may slightly shorten the lifetime of the junction, which is because the molecule will experience an electrostatic force that destabilizes the molecular junction when the direction of the electric dipole of the junction is not collinear with the direction of the current flow.



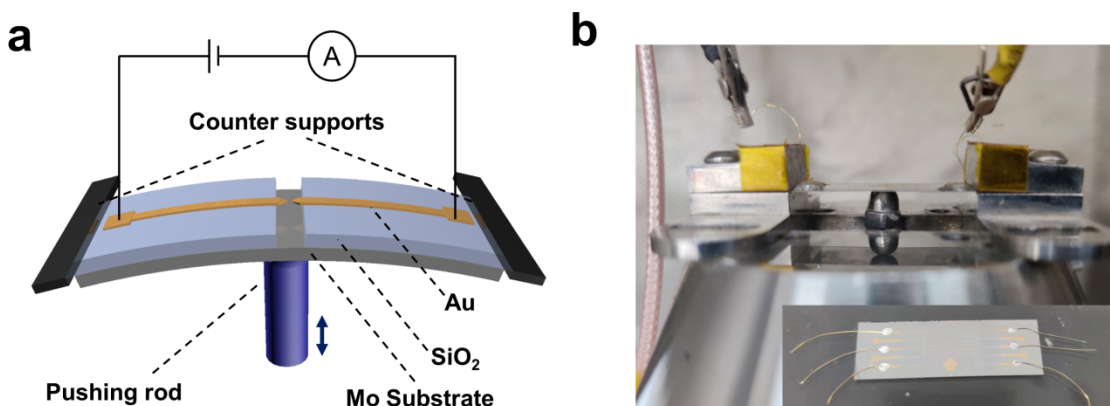


Supplementary Fig. 11 Demonstrations of non-volatile memory behavior in single metallofullerene devices of $\text{Sc}_2\text{C}_2@D_{2d}(23)\text{-C}_{84}$ and $\text{Sc}_2\text{C}_2@C_{2v}(9)\text{-C}_{86}$. **a**, Logarithm-binned 1D histogram and 2D conductance–displacement histogram constructed from the single-molecule conductance measurements under +0.1 V, and the non-volatile memory measurements of $\text{Sc}_2\text{C}_2@D_{2d}(23)\text{-C}_{84}$. **b**, Logarithm-binned 1D histogram and 2D conductance–displacement histogram constructed from the single-molecule conductance measurements under +0.1 V, and the non-volatile memory measurements of $\text{Sc}_2\text{C}_2@C_{2v}(9)\text{-C}_{86}$. In the experiments, +0.8 V (marked as W_1) is used to write the ‘1’ state, -0.8 V (marked as W_0) to write the ‘0’ state, and 0.2 V (marked as R) to read out the digital information through the conductance of the molecule, respectively. To ensure data collection, we treated +0.01 V as 0 (marked as S) to exhibit the non-volatile memory characteristics.

S5 The experiments using mechanically controllable break junction (MCBJ) chip

To demonstrate that the drifting issue in STM-BJ is the main problem limiting the lifetime of molecular junctions, we newly developed a more stable microfabricated mechanically controllable break junction (MCBJ) chip to evaluate the lifetime of molecular junctions.

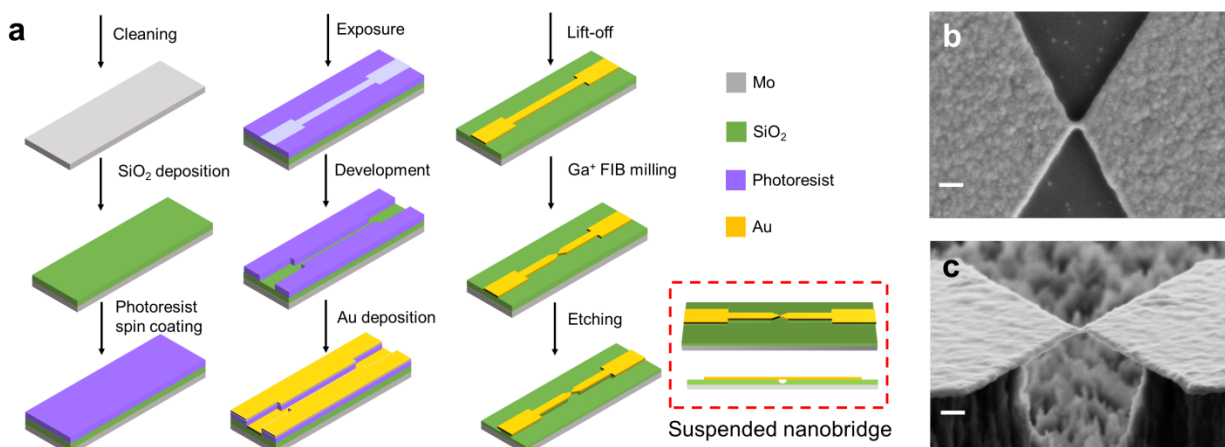
Schematic of mechanically controllable break junction (MCBJ)^{5,6} is shown in **Supplementary Fig. 12a**. A bending substrate was fixed with an underneath pushing rod and two counter supports. With the movement of the pushing rod, the suspended electrode deformed till it broke into an adjustable nanogap, enabling the formation of a single-molecule junction. The photograph of our lab-built MCBJ setup⁷ is shown in **Supplementary Fig. 12b**. We connected the contacting pads of the sample with gold wires (0.1 mm in diameter, Beijing Jiaming Co., Ltd.) via silver conductive paint (SCP03B, Electrolube), as shown in the inset of **Supplementary Fig. 12b**.



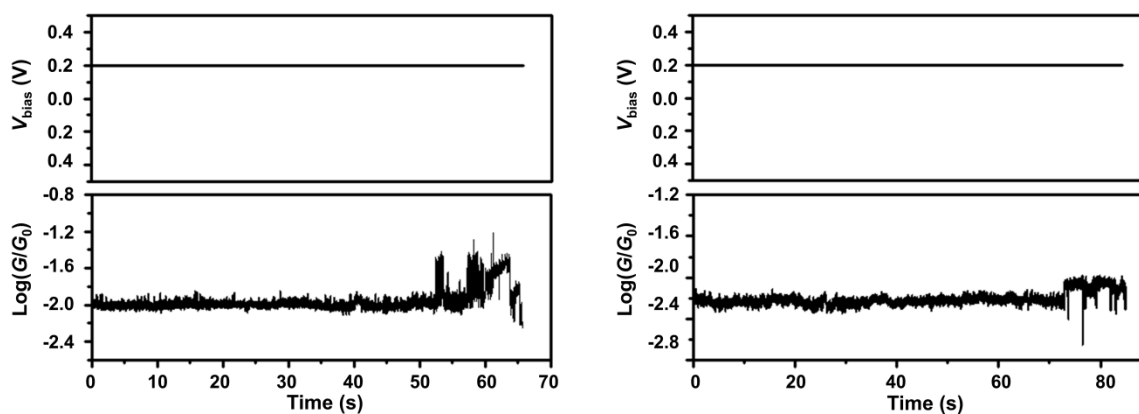
Supplementary Fig. 12 The experiments using mechanically controllable break junction (MCBJ) chip. **a**, Schematic of MCBJ. **b**, Photograph of the MCBJ setup. Inset: Photograph of the microfabricated MCBJ sample.

The samples for MCBJ are fabricated using the flowing procedure, as shown in **Supplementary Fig. 13a**. A polished moly (Mo) substrate (4 inches in diameter and 150 μm in thickness) was cleaned with acetone, ethanol, and deionized water sequentially. An insulating and sacrificial layer of SiO₂ with 2 μm thickness was deposited using plasma-enhanced chemical vapor deposition (SI 500D, Sentech Instruments GmbH). The electrodes patterns with micron linewidth were fabricated via photolithography (MA8BA8, SUSS MicroTec Lithography GmbH). A 50 nm Au film with 3 nm Ti as adhesion layer served as electrodes by electron beam evaporation (DE400, DE Technology Inc.) and lift-off process. The constriction structures were fabricated using Ga⁺ focus ion beam (FIB) milling (Orion Nanofab, Zeiss) to form narrow electrodes with a width of around 80 nm (**Supplementary Fig. 13b**). The suspended structures were realized by plasma etching

(HAASRODE-E200A, Leuven Instruments) and isotropic wet etching using buffered oxide etchant. The SEM image of the suspended nano bridge is shown in **Supplementary Fig. 13c**. We found that the lifetime of the junctions can last for ~ 1 min (**Supplementary Fig. 14**). The much longer lifetime using the MCBJ chip suggests the lifetime of single-molecule junctions could be further improved by some engineering approaches such as microfabrication.



Supplementary Fig. 13 The mechanically controllable break junction chip. **a**, Schematic of the microfabricated samples. **b**, Scanning electron microscope image of the electrode after Ga^+ FIB milling. **c**, Scanning electron microscope image with a 60° tilt angle view of the suspended nano bridge. Scale bar equals 200 nm for **b** and **c**.






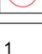
Supplementary Fig. 14 The molecular junction lifetime of $\text{Sc}_2\text{C}_2@\text{Cs}(\text{hept})\text{-C}_{88}$ molecule using MCBJ chip.





S6. The *in-situ* logic-in-memory operations

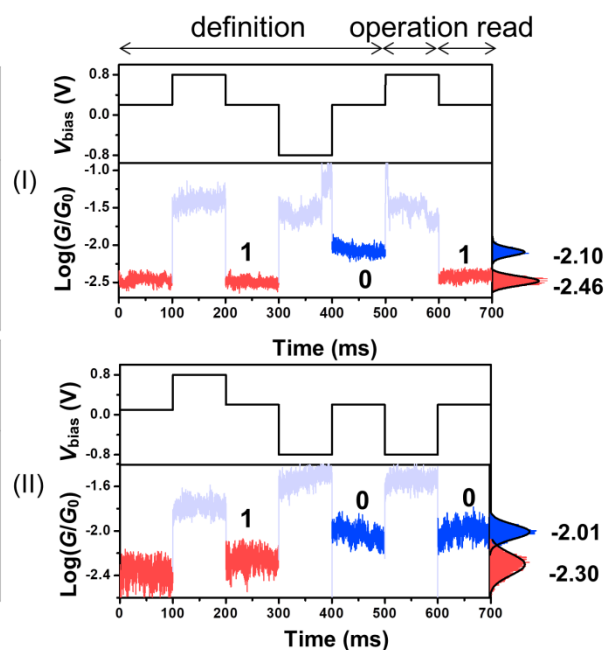
The growing importance of applications based on machine learning and the internet of things is driving the developments of dedicated and energy-efficient electronics. The von Neumann architecture in modern computers is approaching its performance limitations due to the memory wall induced by the separated computation and storage, and thus in-memory computing offers the potential in future computing by processing and storing information in the same two-terminal memory devices. Realizing logic operations in non-volatile memory arrays is a promising approach for developing in-memory computing architectures.

Logic operations have never been demonstrated in the single-molecule non-volatile memory before. Our work presents an experimental model that bridges the gap of single-molecule in-memory computing. The experimental results with LCS corresponding to the state ‘1’ and HCS corresponding to state ‘0’ is shown as **Supplementary Fig. 15**, and the results with HCS corresponding to the state ‘1’ and LCS corresponding to state ‘0’ is shown as **Supplementary Fig. 16**.

a

No.	Cycle 1			Cycle 2	TRUE			
	T_1	T_2	Z'		p	q	Read	Experiment
1	1	0			0	0	1	I
2	1	0			= 1	0	1	I
3	1	0			0	1	1	I
4	1	0			1	1	1	I

No.	Cycle 1			Cycle 2	FLASE			
	T_1	T_2	Z'		p	q	Read	Experiment
5	0	1			0	0	0	II
6	0	1			= 1	0	0	II
7	0	1			0	1	0	II
8	0	1			1	1	0	II



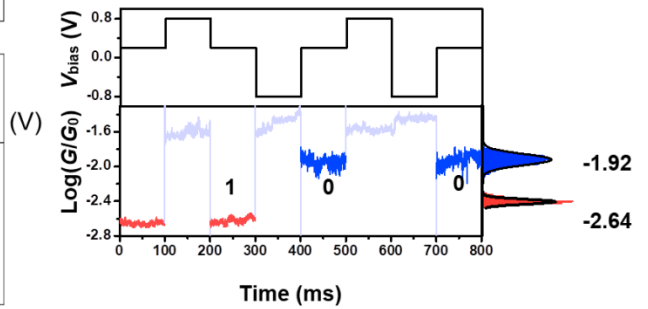
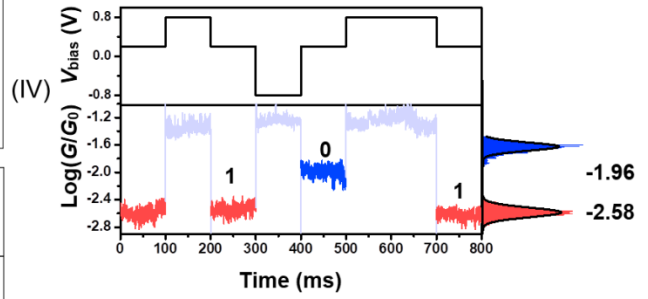
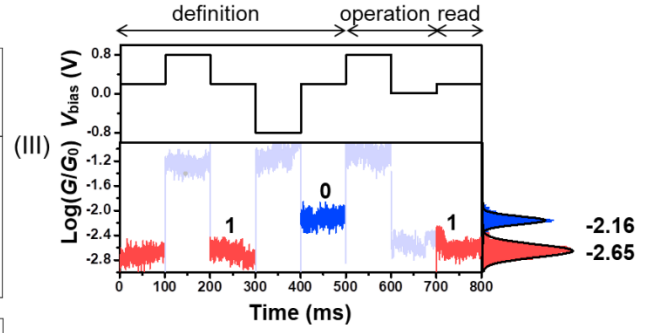
b

No.	Cycle 1			Cycle 2			Cycles 1, 2			
	T_1	T_2	Z'	$T_1 = p$	$T_2 = q$	Z	p	q	Read	Experiment
9	1	0		0	0		0	0	1	III
10	1	0		1	0		1	0	1	IV
11	1	0		0	1		0	1	0	V
12	1	0		1	1		1	1	1	III

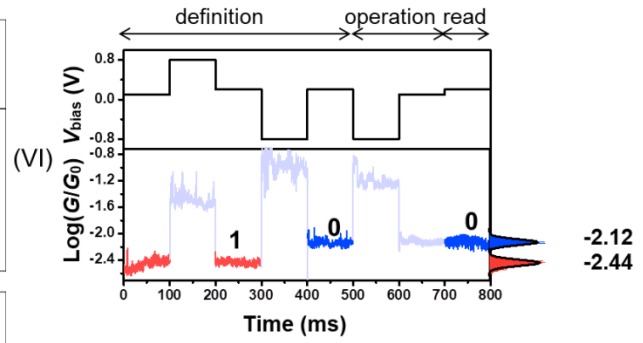
No.	Cycle 1			Cycle 2			Cycles 1, 2			
	T_1	T_2	Z'	$T_1 = p$	$T_2 = q$	Z	p	q	Read	Experiment
13	0	1		0	0		0	0	0	VI
14	0	1		1	0		1	0	0	VII
15	0	1		0	1		0	1	1	VIII
16	0	1		1	1		1	1	0	VI

No.	Cycle 1			Cycle 2			Cycles 1, 2			
	T_1	T_2	Z'	$T_1 = q$	$T_2 = p$	Z	p	q	Read	Experiment
17	1	0		0	0		0	0	1	III
18	1	0		0	1		1	0	0	V
19	1	0		1	0		0	1	1	IV
20	1	0		1	1		1	1	1	III

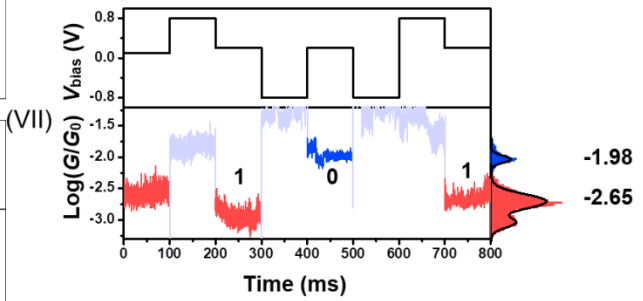
No.	Cycle 1			Cycle 2			Cycles 1, 2			
	T_1	T_2	Z'	$T_1 = p$	$T_2 = 1$	Z	p	q	Read	Experiment
21	1	0		0	1		0	0	0	V
22	1	0		1	1		1	0	1	III
23	1	0		0	1		0	1	0	V
24	1	0		1	1		1	1	1	III



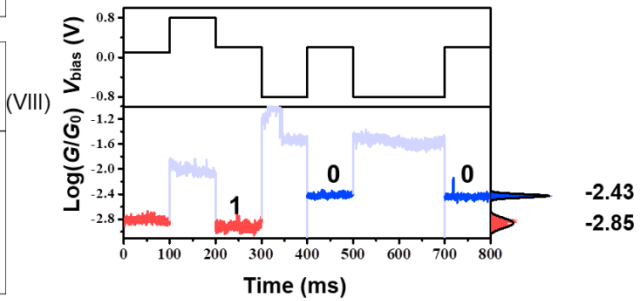
No.	Cycle 1			Cycle 2			Cycles 1, 2			
	T_1	T_2	Z'	$T_1=q$	$T_2=1$	Z	p	q	Read	Experiment
25	1	0		0	1		0	0	0	V
26	1	0		0	1		= 1	0	0	V
27	1	0		1	1		0	1	1	III
28	1	0		1	1		1	1	1	III



No.	Cycle 1			Cycle 2			Cycles 1, 2			
	T_1	T_2	Z'	$T_1=q$	$T_2=p$	Z	p	q	Read	Experiment
29	0	1		0	0		0	0	0	VI
30	0	1		0	1		= 1	0	0	VIII
31	0	1		1	0		0	1	1	VII
32	0	1		1	1		1	1	0	VI



No.	Cycle 1			Cycle 2			Cycles 1, 2			
	T_1	T_2	Z'	$T_1=1$	$T_2=p$	Z	p	q	Read	Experiment
33	0	1		1	0		0	0	1	VII
34	0	1		1	1		= 1	0	0	VI
35	0	1		1	0		0	1	1	VII
36	0	1		1	1		1	1	0	VI



No.	Cycle 1			Cycle 2			Cycles 1, 2			
	T_1	T_2	Z'	$T_1=1$	$T_2=q$	Z	p	q	Read	Experiment
37	0	1		1	0		0	0	1	VII
38	0	1		1	0		= 1	0	1	VII
39	0	1		1	1		0	1	0	VI
40	0	1		1	1		1	1	0	VI

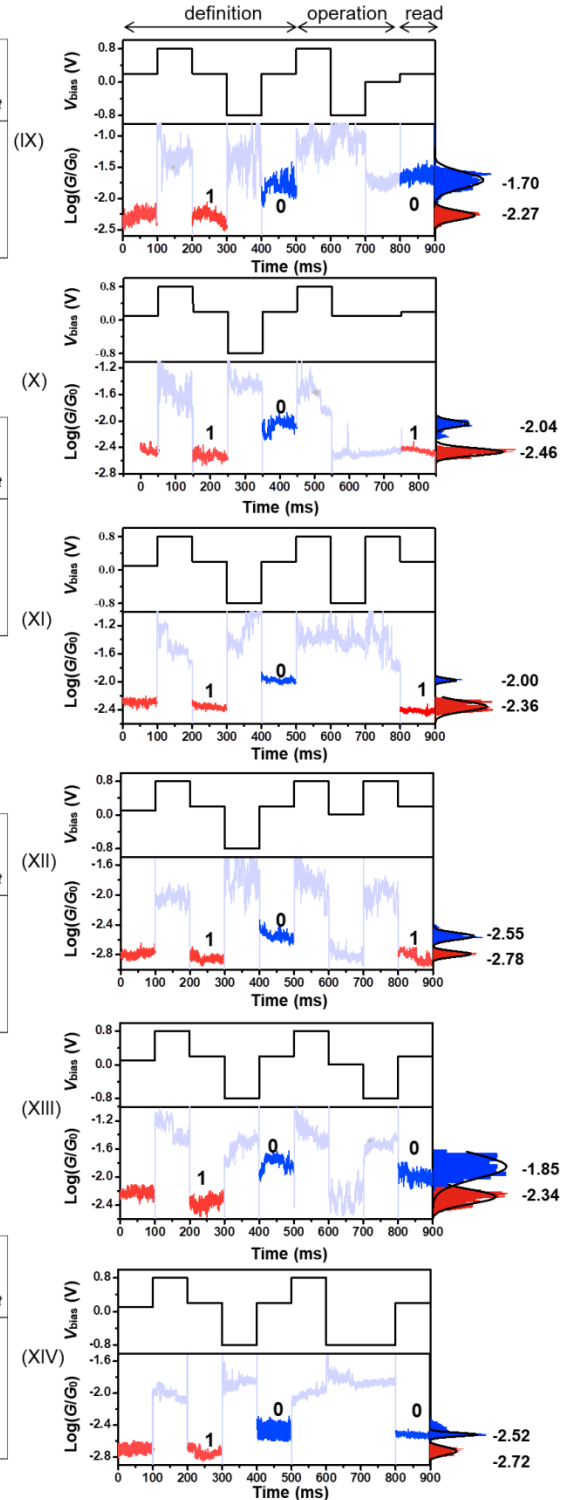
C

NO.	Cycle 1			Cycle 2			Cycle 3			Cycles 1,2,3 p OR q			
	T_1	T_2	Z'	$T_1=p$	$T_2=1$	Z_1	$T_1=q$	$T_2=0$	Z_2	p	q	Read	Experiment
41	1	0		0	1		0	0		0	0	0	IX
42	1	0		1	1		0	0		1	0	1	X
43	1	0		0	1		1	0		0	1	1	XI
44	1	0		1	1		1	0		1	1	1	XII

NO.	Cycle 1			Cycle 2			Cycle 3			Cycles 1,2,3 p NAND q			
	T_1	T_2	Z'	$T_1=0$	$T_2=q$	Z_1	$T_1=1$	$T_2=p$	Z_2	p	q	Read	Experiment
45	1	0		0	0		1	0		0	0	1	XII
46	1	0		0	0		1	1		1	0	1	X
47	1	0		0	1		1	0		0	1	1	XI
48	1	0		0	1		1	1		1	1	0	IX

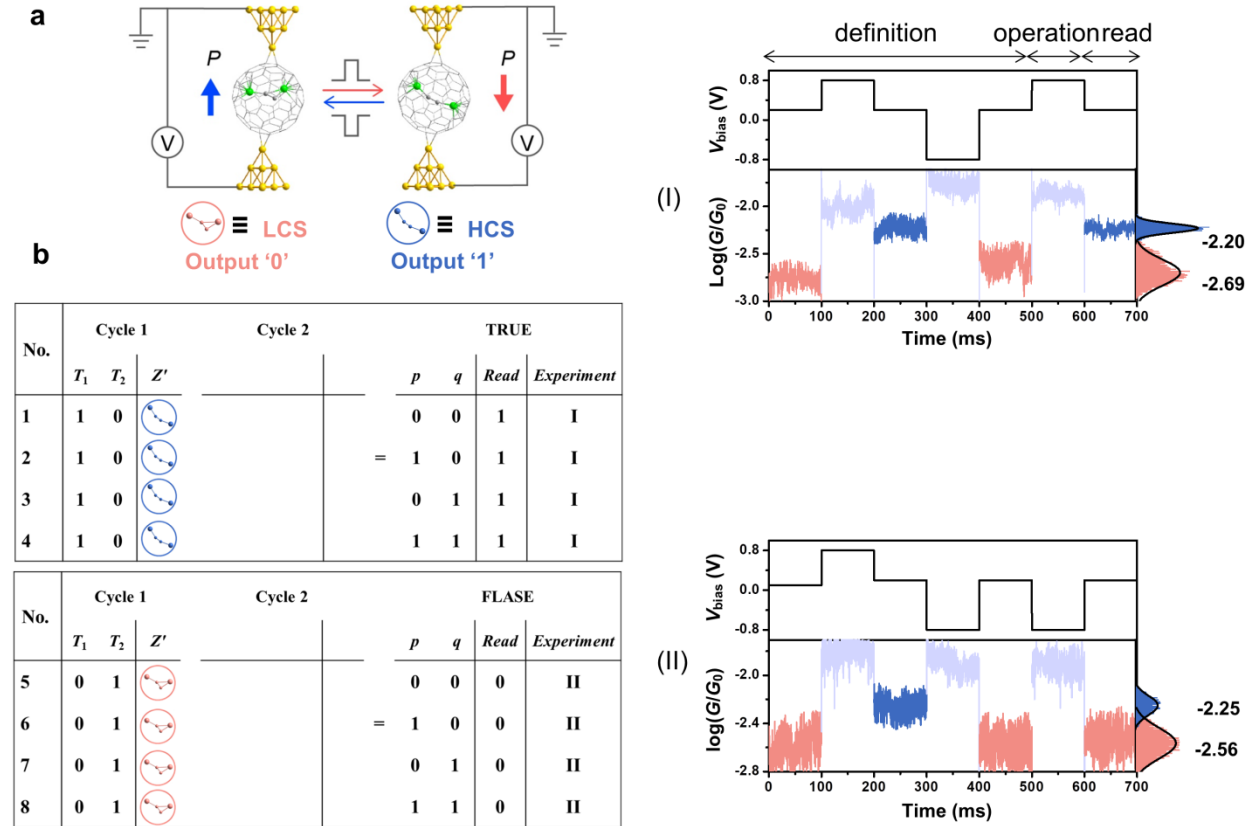
NO.	Cycle 1			Cycle 2			Cycle 3			Cycles 1,2,3 p NOR q			
	T_1	T_2	Z'	$T_1=0$	$T_2=q$	Z_1	$T_1=0$	$T_2=p$	Z_2	p	q	Read	Experiment
49	1	0		0	0		0	0		0	0	1	X
50	1	0		0	0		0	1		1	0	0	XIII
51	1	0		0	1		0	0		0	1	0	IX
52	1	0		0	1		0	1		1	1	0	XIV

NO.	Cycle 1			Cycle 2			Cycle 3			Cycles 1,2,3 p AND q			
	T_1	T_2	Z'	$T_1=p$	$T_2=1$	Z_1	$T_1=q$	$T_2=1$	Z_2	p	q	Read	Experiment
53	1	0		0	1		0	1		0	0	0	XIV
54	1	0		1	1		0	1		1	0	0	XIII
55	1	0		0	1		1	1		0	1	0	IX
56	1	0		1	1		1	1		1	1	1	X



Supplementary Fig. 15 *In-situ* demonstration of the fourteen basic Boolean logic operation. **a**, The pulse bias sequences (I) and (II) for TRUE and FALSE have one operation cycle. **b**, The pulse bias sequences (III)-(VIII) for RIMP, NIMP etc, have two operation cycles. **c**, The pulse bias sequences (IX) to (XIV) for OR, AND etc, have three operation cycles. There are 14 Boolean logic operations with 56 functions, which can be

represented by 14 independent pulse sequences. The initial characterization cycle is performed prior to the logic operations to define the conductance values of the states ‘0’ and ‘1’ as shown in the “definition” regime. After that, a pulse bias sequences are applied in the “operation” regime to execute the logic operation, followed by a “read” voltage to read out the logic value. (Left) The truth tables show the sequence of operations to the implication functions. (Right) The experimental demonstration of logic operation. Here, the low conductance state (LCS) corresponds to the state ‘1’, the same as in Fig. 3 in the main text.



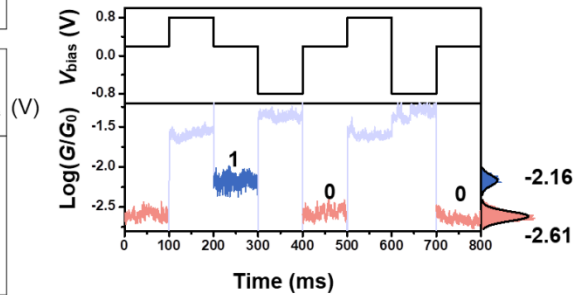
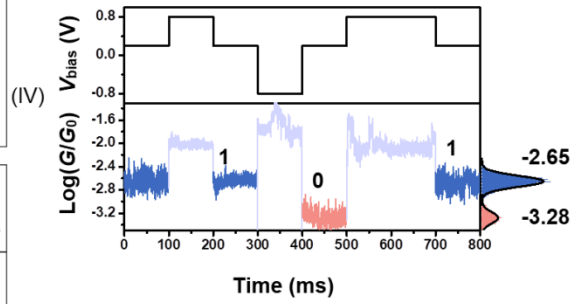
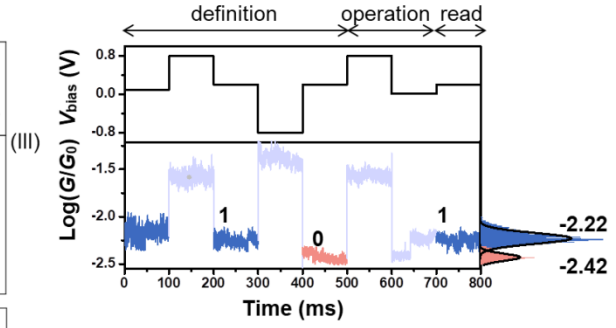
c

No.	Operation Cycles						Cycles 1, 2			
	Cycle 1			Cycle 2			p	q	Read	Experiment
	T_1	T_2	Z'	$T_1=p$	$T_2=q$	Z				
9	1	0		0	0		0	0	1	III
10	1	0		1	0		=	1	0	IV
11	1	0		0	1			0	1	V
12	1	0		1	1			1	1	III

No.	Cycle 1			Cycle 2			Cycles 1, 2			
	T_1	T_2	Z'	$T_1=p$	$T_2=q$	Z	p	q	Read	Experiment
13	0	1		0	0		0	0	0	VI
14	0	1		1	0		=	1	0	VII
15	0	1		0	1			0	1	VIII
16	0	1		1	1			1	1	VI

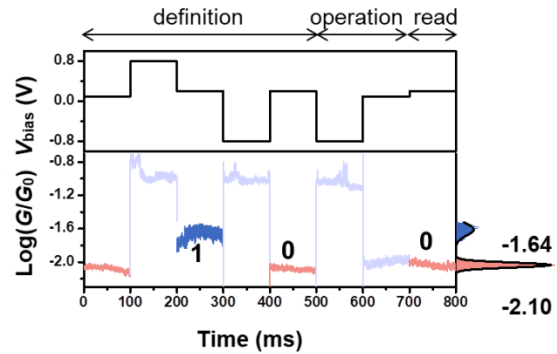
No.	Cycle 1			Cycle 2			Cycles 1, 2			
	T_1	T_2	Z'	$T_1=q$	$T_2=p$	Z	p	q	Read	Experiment
17	1	0		0	0		0	0	1	III
18	1	0		0	1		=	1	0	V
19	1	0		1	0			0	1	IV
20	1	0		1	1			1	1	III

No.	Cycle 1			Cycle 2			Cycles 1, 2			
	T_1	T_2	Z'	$T_1=p$	$T_2=1$	Z	p	q	Read	Experiment
21	1	0		0	1		0	0	0	V
22	1	0		1	1		=	1	0	III
23	1	0		0	1			0	1	V
24	1	0		1	1			1	1	III



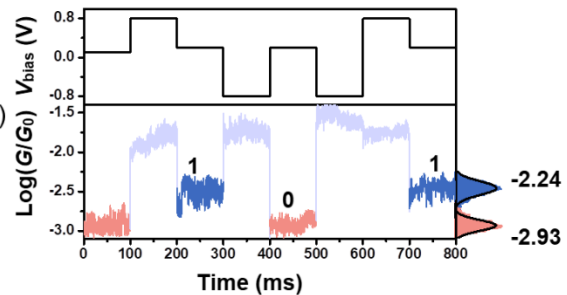
No.	Cycle 1			Cycle 2			Cycles 1, 2			
	T_1	T_2	Z'	$T_1=q$	$T_2=1$	Z	p	q	Read	Experiment
25	1	0		0	1		0	0	0	V
26	1	0		0	1		1	0	0	V
27	1	0		1	1		0	1	1	III
28	1	0		1	1		1	1	1	III

(VI)



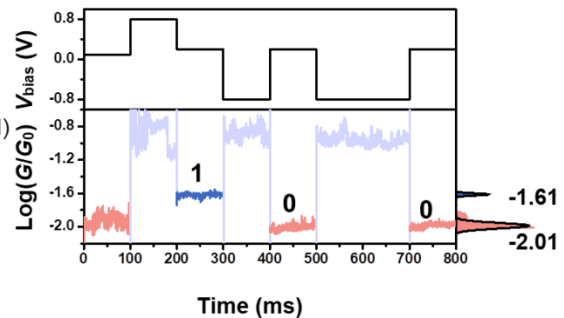
No.	Cycle 1			Cycle 2			Cycles 1, 2			
	T_1	T_2	Z'	$T_1=q$	$T_2=p$	Z	p	q	Read	Experiment
29	0	1		0	0		0	0	0	VI
30	0	1		0	1		1	0	0	VIII
31	0	1		1	0		0	1	1	VII
32	0	1		1	1		1	1	0	VI

(VII)



No.	Cycle 1			Cycle 2			Cycles 1, 2			
	T_1	T_2	Z'	$T_1=1$	$T_2=p$	Z	p	q	Read	Experiment
33	0	1		1	0		0	0	1	VII
34	0	1		1	1		1	0	0	VI
35	0	1		1	0		0	1	1	VII
36	0	1		1	1		1	1	0	VI

(VIII)



No.	Cycle 1			Cycle 2			Cycles 1, 2			
	T_1	T_2	Z'	$T_1=1$	$T_2=q$	Z	p	q	Read	Experiment
37	0	1		1	0		0	0	1	VII
38	0	1		1	0		1	0	1	VII
39	0	1		1	1		0	1	0	VI
40	0	1		1	1		1	1	0	VI

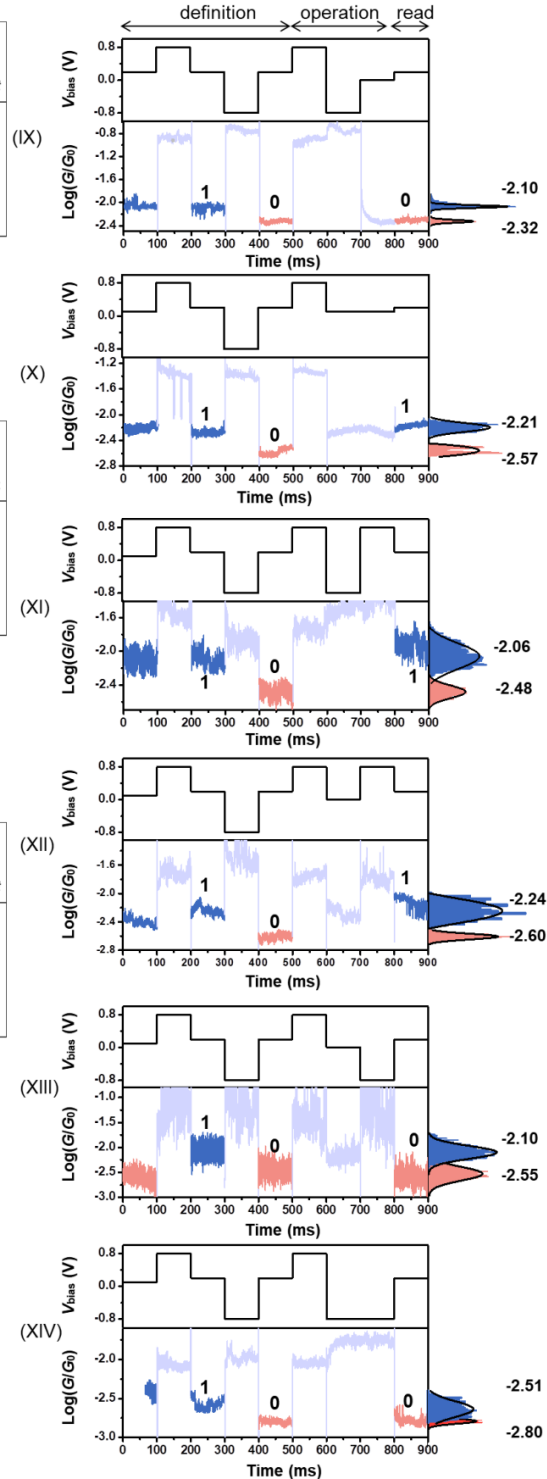
d

No.	Cycle 1			Cycle 2			Cycle 3			Cycles 1,2,3 p OR q			
	T_1	T_2	Z'	$T_1=p$	$T_2=1$	Z_1	$T_1=q$	$T_2=0$	Z_2	p	q	Read	Experiment
41	1	0		0	1		0	0		0	0	0	IX
42	1	0		1	1		0	0		1	0	1	X
43	1	0		0	1		1	0		0	1	1	XI
44	1	0		1	1		1	0		1	1	1	XII

No.	Cycle 1			Cycle 2			Cycle 3			Cycles 1,2,3 p NAND q			
	T_1	T_2	Z'	$T_1=0$	$T_2=q$	Z_1	$T_1=1$	$T_2=p$	Z_2	p	q	Read	Experiment
45	1	0		0	0		1	0		0	0	1	XII
46	1	0		0	0		1	1		1	0	1	X
47	1	0		0	1		1	0		0	1	1	XI
48	1	0		0	1		1	1		1	1	0	IX

No.	Cycle 1			Cycle 2			Cycle 3			Cycles 1,2,3 p NOR q			
	T_1	T_2	Z'	$T_1=0$	$T_2=q$	Z_1	$T_1=0$	$T_2=p$	Z_2	p	q	Read	Experiment
49	1	0		0	0		0	0		0	0	1	X
50	1	0		0	0		0	1		1	0	0	XIII
51	1	0		0	1		0	0		0	1	0	IX
52	1	0		0	1		0	1		1	1	0	XIV

No.	Cycle 1			Cycle 2			Cycle 3			Cycles 1,2,3 p AND q			
	T_1	T_2	Z'	$T_1=p$	$T_2=1$	Z_1	$T_1=q$	$T_2=1$	Z_2	p	q	Read	Experiment
53	1	0		0	1		0	1		0	0	0	XIV
54	1	0		1	1		0	1		1	0	0	XIII
55	1	0		0	1		1	1		0	1	0	IX
56	1	0		1	1		1	1		1	1	1	X



Supplementary Fig. 16 Logic tables and *in-situ* demonstration of the fourteen basic Boolean logic operation. (Left) The truth tables show the sequence of operations to the implication functions. (Right) The experimental demonstration of logic operation. Here, the Boolean logic operation is the same as those shown in **Supplementary Fig. 15**, while the high conductance state (HCS) corresponds to the state ‘1’.

Supplementary Table 1. Computational Universality of IMP (Material Implication), TRUE and FALSE Operations: the 14 distinct binary Boolean operations on two logic values.

operation	Truth Table				Implication function
p	0	1	0	1	$= p$
q	0	0	1	1	$= q$
TRUE	1	1	1	1	$= (1 \text{ RIMP } 0) \cdot Z' + (1 \text{ NIMP } 0) \cdot (\text{not } Z')$
FALSE	0	0	0	0	$= (0 \text{ RIMP } 1) \cdot Z' + (0 \text{ NIMP } 1) \cdot (\text{not } Z')$
$p \text{ IMP } q$	1	0	1	1	$= (q \text{ RIMP } p) \cdot (Z' = 1)$
$p \text{ NIMP } q$	0	1	0	0	$= (p \text{ NIMP } q) \cdot (\text{not } Z' = 0)$
$p \text{ RIMP } q$	1	1	0	1	$= (p \text{ RIMP } q) \cdot (Z' = 1)$
$p \text{ RNIMP } q$	0	0	1	0	$= (q \text{ NIMP } p) \cdot (\text{not } Z' = 0)$
p	0	1	0	1	$= (p \text{ RIMP } 1) \cdot (Z' = 1)$
not p	1	0	1	0	$= (1 \text{ NIMP } p) \cdot (\text{not } Z' = 0)$
q	0	0	1	1	$= (q \text{ RIMP } 1) \cdot (Z' = 1)$
not q	1	1	0	0	$= (1 \text{ NIMP } p) \cdot (\text{not } Z' = 0)$
$p \text{ OR } q$	0	1	1	1	$= (q \text{ RIMP } 0) \cdot p + (q \text{ NIMP } 0) \cdot (\text{not } p)$
$p \text{ NAND } q$	1	1	1	0	$= (1 \text{ RIMP } p) \cdot (\text{not } q) + (1 \text{ NIMP } p) \cdot q$
$p \text{ NOR } q$	1	0	0	0	$= (0 \text{ RIMP } p) \cdot (\text{not } q) + (0 \text{ NIMP } p) \cdot q$
$p \text{ AND } q$	0	0	0	1	$= (q \text{ RIMP } 1) \cdot p + (q \text{ NIMP } 1) \cdot (\text{not } p)$
$p \text{ XOR } q$	0	1	1	0	$= (p \text{ OR } q) \& (p \text{ NAND } q)$ (Not implemented in this work)
$p \text{ XNOR } q$	1	0	0	1	$= (p \text{ IMP } q) \& (p \text{ RIMP } q)$ (Not implemented in this work)

Two functions cannot be realized with a single bipolar resistive switch: XOR and XNOR.⁸ As XOR, for example, a combination of NIMP and RNIMP after a FALSE operation would lead to XOR,

$$Z_{1,\text{cycle}} = \text{FALSE} \quad (2)$$

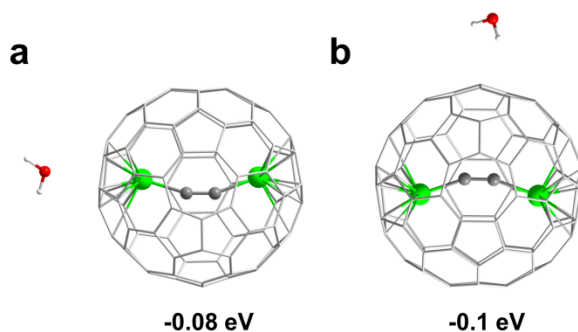
$$Z_{2,\text{cycle}} = p \text{ NIMP } q \quad (3)$$

$$Z_{3,\text{cycle}} = (p \text{ XNOR } q) = (p \text{ RNIMP } q) \quad (4)$$

but since the whole equation $Z = (T_1 \text{ RIMP } T_2) \cdot Z' + (T_1 \text{ NIMP } T_2) \cdot (\text{not } Z')$ (1) in main text must be considered in a third cycle, hence, $Z_{3,\text{cycle}} = (q \text{ RIMP } p) \cdot (p \text{ NIMP } q) + (q \text{ NIMP } p) \cdot (\text{not}(p \text{ NIMP } q))$ (5)

is also should be satisfied. In the case of $p = '1'$ and $q = '0'$, a back-switching to $Z = 0$ occurs in the third cycle preventing an XOR operation. Due to this property, no function which requires switching if $p \neq q$ can be implemented with a single device. Thus, if these functions are needed, two devices must be connected via a wired AND. For XNOR, one cell performs IMP and the other RIMP, namely, $Z = p \text{ XNOR } q = (p \text{ IMP } q) \& (p \text{ RIMP } q)$; And XOR can be realized by OR and NAND: $Z = p \text{ XOR } q = (p \text{ OR } q) \& (p \text{ NAND } q)$.

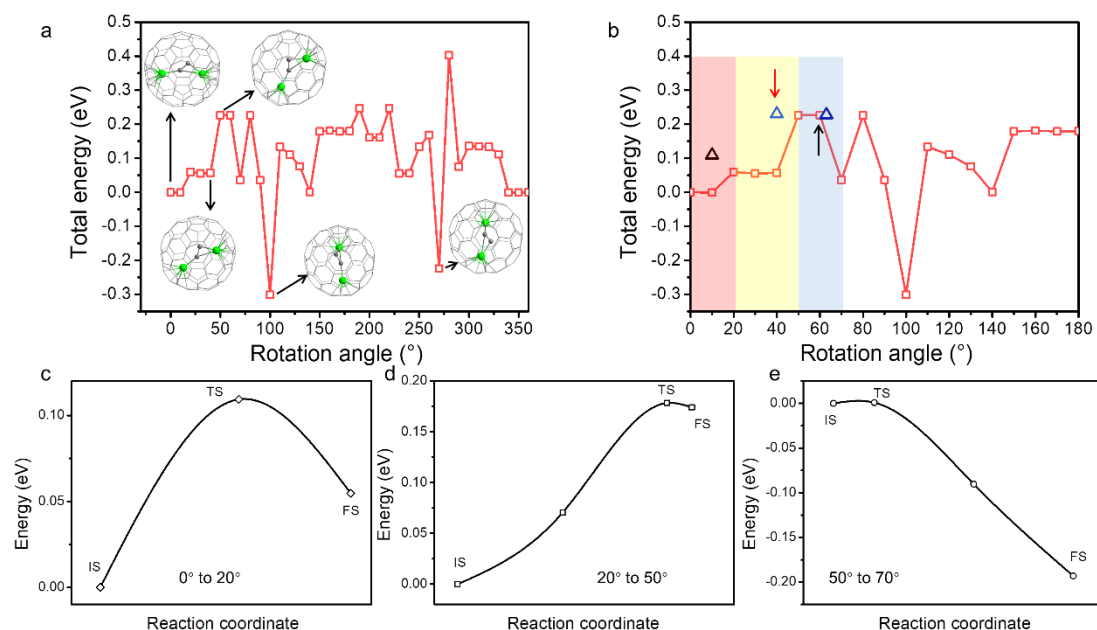
S7. Theoretical Calculation and Simulation



Supplementary Fig. 17. The binding energy between the water molecules and Sc₂C₂@Cs(hept)-C₈₈ with opposite dipole towards the molecule. **a**, The water molecule is adsorbed at the top position. **b**, The water molecule is adsorbed at the side position.

To rule out the possibility that the hysteresis loops shown in **Supplementary Fig. 3a-3b** come from the dipoles of adsorbates on the fullerene cage surface, we calculated the binding energy between them. Therefore, we placed one single water molecule at two different positions (top and side), and then the binding energy between water and Sc₂C₂@Cs(hept)-C₈₈ is calculated after relaxation. **Supplementary Fig. 17** shows that the binding energy of the water molecule at the two positions is -0.1 eV and -0.08 eV, respectively. The relatively small binding energy (~ 0.1 eV) suggests that the coupling between the water molecule and fullerene is rather weak, indicating that the water molecule can be desorbed from the C₈₈ cage easily. As a result, the dipole adsorbates on the fullerene cage surface cannot induce the hysteresis loops and two-conduction-state switching.

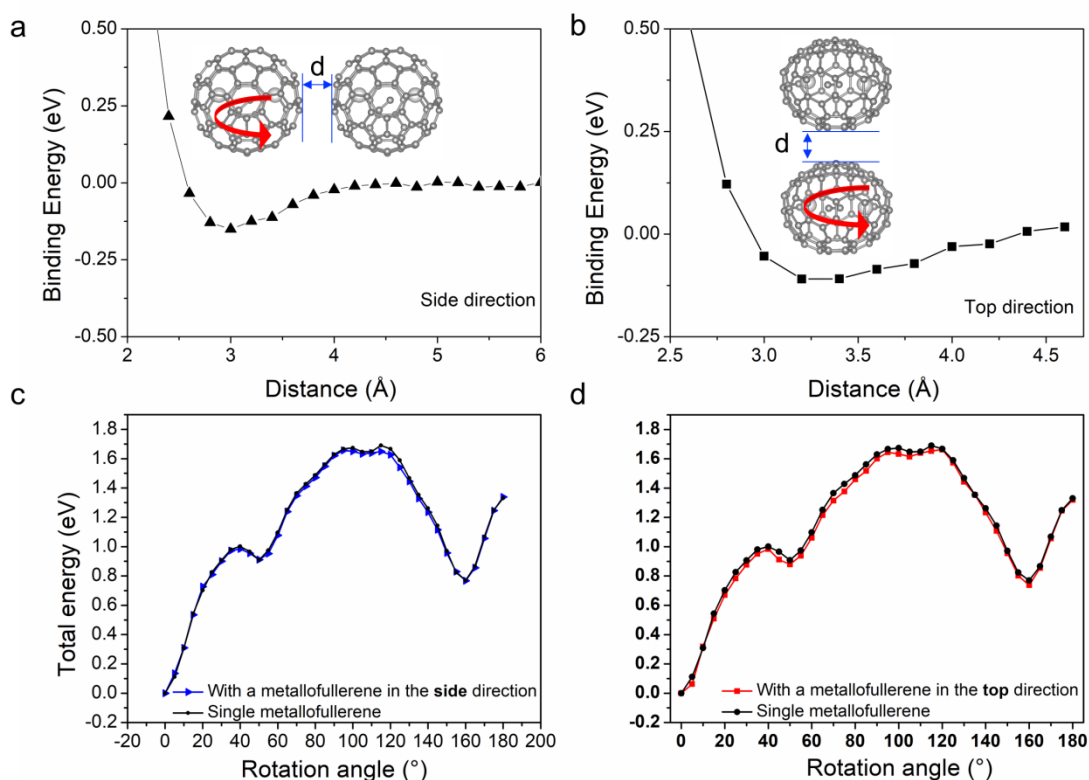
The transition states (TS) were calculated using a damped molecular dynamics algorithm combined with the climbing-image nudged elastic band (CI-NEB) method within the Vienna Ab initio Simulation Package (VASP 5.4.4). In the case of Sc₂C₂@Cs(hept)-C₈₈, the rotation region from 0° to 70° is selected to obtain the TS with a barrier of around 0.227 eV. However, because of the complex degrees of freedom of [Sc₂C₂] cluster in the cage, there are numerous local minima on the energy potential surface, even if [Sc₂C₂] cluster moves in a small region. To address this issue, three regions are chosen to obtain the TS, namely, 0° to 20°, 20° to 50° and 50° to 70°. Three TSs with 0.109 eV, 0.2305 eV, and 0.2276 eV were obtained in the 0° to 20°, 20° to 50° and 50° to 70° region, respectively (triangle in **Supplementary Fig. 18b**). As a result, a slightly higher energy barrier (0.231 eV) is required to be overcome when the [Sc₂C₂] cluster is rotated from 0° to 70°.



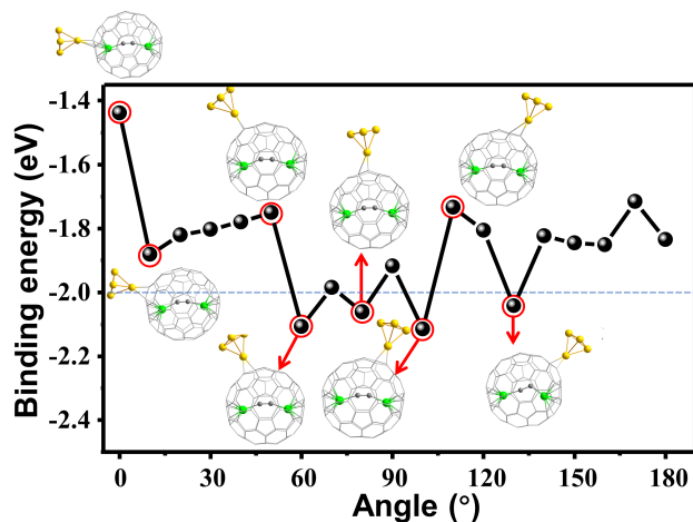
Supplementary Fig. 18 | The calculated energy profile and binding energy versus rotation angle of the cage with $[\text{Sc}_2\text{C}_2]$. **a**, The energy profile versus rotation angle about an axis perpendicular to the long axis of the $[\text{Sc}_2\text{C}_2]$ cluster. **b**, The transition states (TS) were calculated in the three regions indicated by the red, yellow, and blue shaded areas, respectively. **c-e**, the transition state (TS) calculated in the 0° to 20° , 20° to 50° and 50° to 70° zone indicated by red, yellow and blue shaded area in **b** respectively. IS and FS indicate initial and final states. Using the energy of IS in each zone as a reference, three TS energies 0.109 eV, 0.178 eV, and 0.0008 eV were obtained by VASP respectively. After adding them to the corresponding energy of 0° , 20° and 50° in **b**, the energy of the three TS energies are 0.109 eV, 0.231 eV and 0.228 eV corresponding to the triangles in **b**. The true energy barrier (indicated by the red arrow) is slightly higher than our lower bound (black arrow).

“The effect of interactions with nearby metallofullerenes is also an intriguing and relevant topic. To clarify the influence of an adjacent fullerene on the transformation of the $[\text{Sc}_2\text{C}_2]$ cluster in the C_{88} cage, two typical orientations relative to the rotation direction are chosen in our calculation, namely ‘side’ and ‘top’ relative to the rotation path (Supplementary Fig. 19a-19b). First, the binding energy evolution as a function of the distance between the two fullerenes is evaluated. The binding energy of 0.1 eV to 0.2 eV (2.3 kcal/mol to 4.6 kcal/mol) is found at a Van der Waals distance ($\sim 3.0\text{\AA}$). The energy profile is then evaluated using these two ‘optimal’ dimers. As shown in Supplementary Fig. 19d, the adjacent fullerene lowers the energy barrier

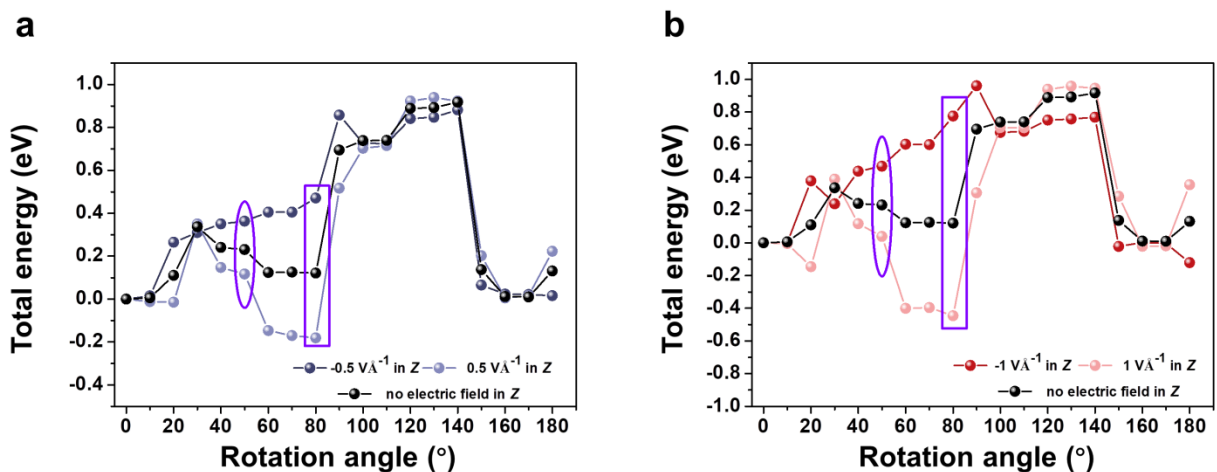
slightly at certain rotation angles (the nearby region of 100°). This is due to the adjacent fullerene only influencing a small part of the rotation path. On the other hand, the energy barriers are slightly lowered over nearly the whole rotation region (Supplementary Fig. 19c). Overall, the interaction between adjacent fullerenes is expected to have a role in slightly lowering the energy barrier, which could facilitate the transformation of the two states in C_{88} cage but not sufficient to allow the two states to transition spontaneously.”



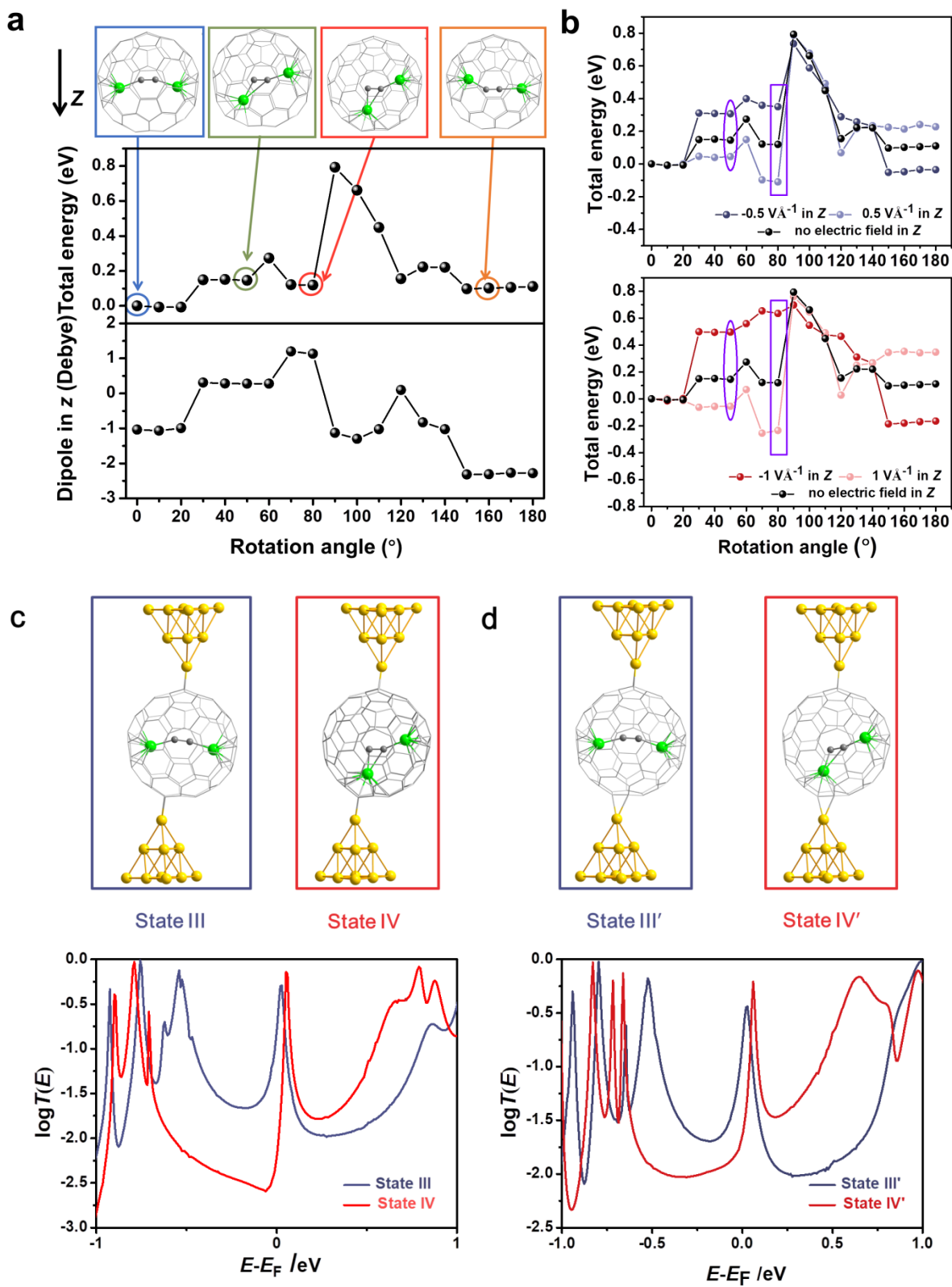
Supplementary Fig. 19| The influence of adjacent fullerene on the energy barrier of the rotation of $[Sc_2C_2]$ cluster in C_{88} cage. a, the binding energy as a function of the distance between these them when the adjacent fullerene is in the rotating direction. b, the binding energy as a function of the distance between these them when the adjacent fullerene is not in the rotating direction. c, the energy profile as the rotation angle without and with the adjacent fullerene on the side of the rotating direction. d, the energy profile as the rotation angle without and with the adjacent fullerene on top of the rotating direction.



Supplementary Fig. 20 The binding energy versus rotation angle of the cage with $[\text{Sc}_2\text{C}_2]$. The binding energy indicates that the configurations are relatively stable when the rotation angles are 60° , 80° , and 130° which were adopted to proceed with further calculations. Due to the symmetry of the molecule, the 60° and 100° configurations are the same. The 60° configurations has the lowest energy and is displayed in the manuscript.

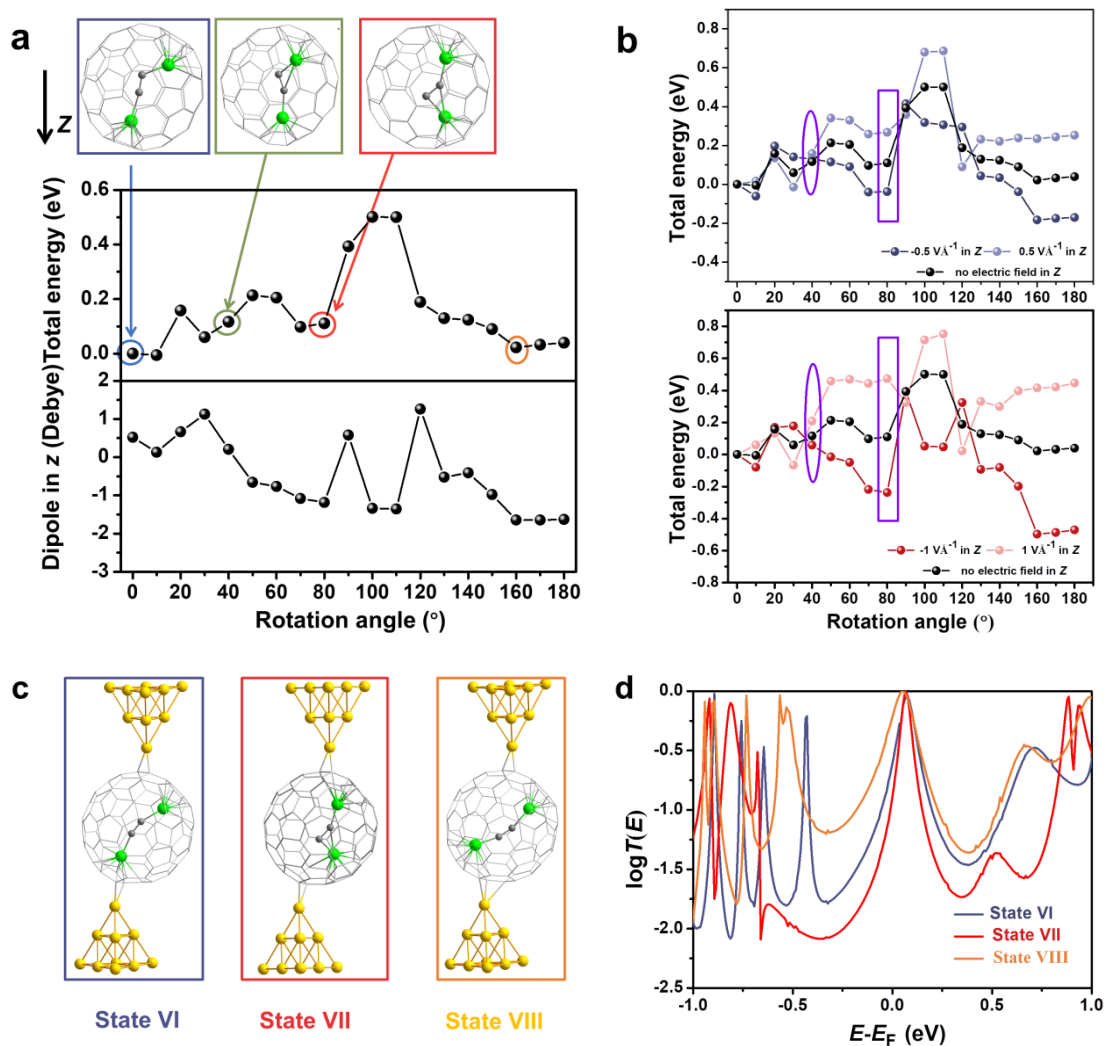


Supplementary Fig. 21 The energy profile versus rotating $[\text{Sc}_2\text{C}_2]$ cluster for rotation 60 degrees in **Supplementary Fig. 20**. **a**, the energy profile after applying $0.5 \text{ V}/\text{\AA}$ in the $\pm z$ direction. **b**, the energy profile after applying $1 \text{ V}/\text{\AA}$ in the $\pm z$ direction.



Supplementary Fig. 22 The energy profile versus rotating $[\text{Sc}_2\text{C}_2]$ cluster for rotation 80 degrees in Supplementary Fig. 20, and the transport function of the stable junction geometries. a, Fully relaxed

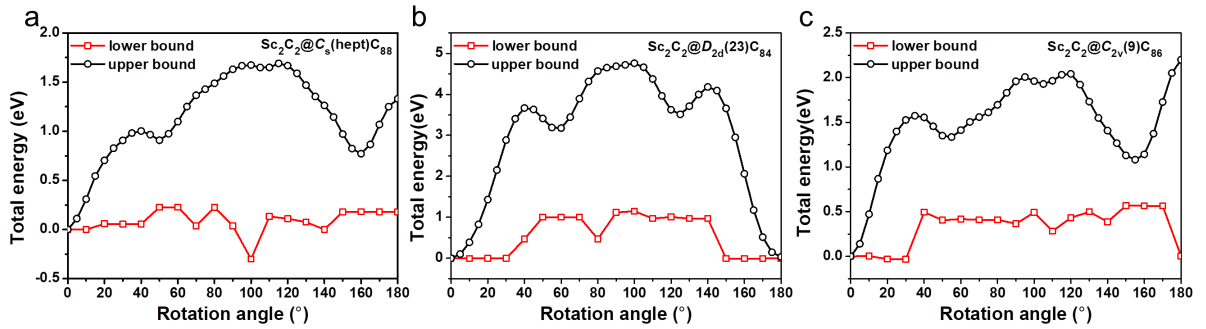
energy profile and the dipole moment in z -direction when rotating $[\text{Sc}_2\text{C}_2]$ cluster from 0° to 180° . From the rotating angle energy profile, three local minimums are identified, namely, 0° (State III), 80° (State IV), and 160° (State V). The z -direction dipole moment at 0° , 80° , and 160° are around -1 Debye, 1.12 Debye, and -2.31 Debye, respectively. And the Z -direction dipole moment at 50° is close to zero, which can be regarded as the intermediate state M_2 . **b**, The energy profile after applying 0.5 V/\AA and 1 V/\AA in the $\pm z$ direction. All the states IV, V, and M_2 respond to the electric field. Due to the opposite dipole direction, states III and IV respond to the electric field in opposite ways. When the positive electric field is applied, the cluster prefers to stay at states III and V while the energy of State IV decreases under a negative electric field. The energy barrier decreases as increasing the electric field. When the electric field is up to 1 V/\AA , the energy barrier goes to about 0, and State IV has the lowest energy, indicating that states III and V can switch to State IV under a negative threshold electric field. **c-d**, Connecting the bottom electrode and C_{88} cage with different connectivity and related transport functions.



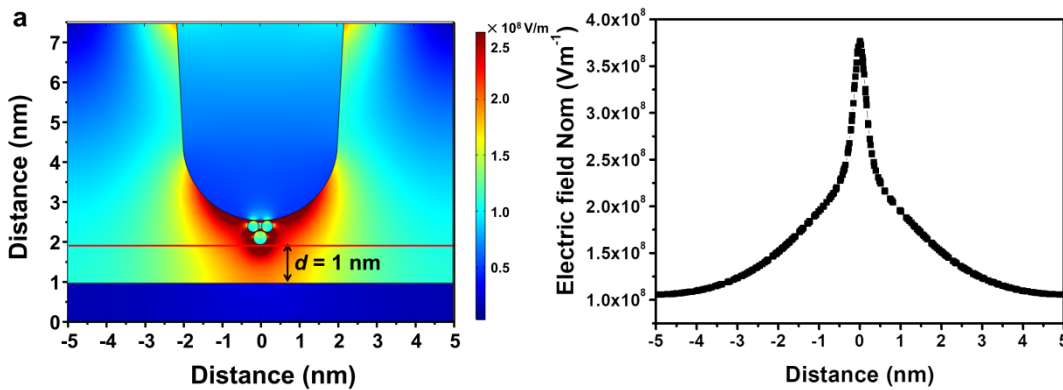
Supplementary Fig. 23 | The energy profile versus rotating $[\text{Sc}_2\text{C}_2]$ cluster for rotation 130° in Supplementary Fig. 20, and the transport function of the stable junction geometries. **a**, Fully relaxed

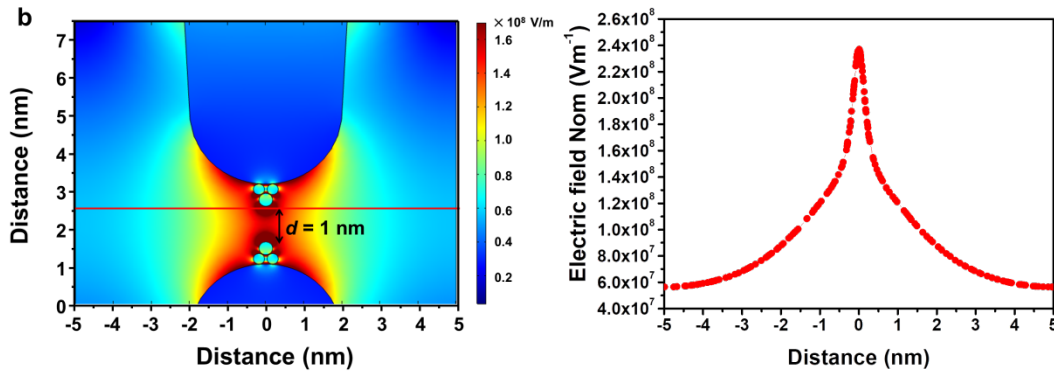
energy profile and the dipole moment in z -direction when rotating $[\text{Sc}_2\text{C}_2]$ cluster from 0° to 180° . From the rotating angle energy profile, three local minimums are identified, namely, 0° (State VI), 80° (State VII), and 160° (State VIII). The Z -direction dipole moment at 0° , 80° , and 160° are around 0.52 Debye, -1.18 Debye and -1.64 Debye, respectively. The z -direction dipole moment at 40° is close to zero, which can be regarded as the intermediate state M_3 . **b**, The energy profile after applying 0.5 V/\AA and 1 V/\AA in the $\pm z$ direction. All the states VII, VIII, and M_3 respond to the electric field. Due to the opposite dipole direction, states VI and VII respond to the electric field in opposite ways. When the negative electric field is applied, the cluster prefers to stay at State VI while the energy of states VII and VIII decreases under an opposite electric field. The energy barrier decreases as increasing the electric field. When the electric field is up to 1 V/\AA , the energy barrier goes to about 0, and states VII and VIII have the lower energy, indicating that State VI can switch to states VII and VIII under a negative threshold electric field. **c-d**, The junction geometries and their related transport function versus electron energy for 0° , 80° , and 160° .

To demonstrate that energy barriers are increased when the fullerene cage is not allowed to fully relax, Fig. 24 shows the energy landscape due to rotation of the $[\text{Sc}_2\text{C}_2]$ cluster, when the cage is held rigid.



Supplementary Fig.24 The calculated energy profile versus rotation angles of $[\text{Sc}_2\text{C}_2]$ cluster in the fullerene cages. **a**, $\text{Sc}_2\text{C}_2@C_s(\text{hept})-C_{88}$. **b**, $\text{Sc}_2\text{C}_2@D_{2d}(23)-C_{84}$. **c**, $\text{Sc}_2\text{C}_2@C_{2v}(9)-C_{86}$. The lower and upper bound rotation energy barriers are presented by the red and black curves respectively.

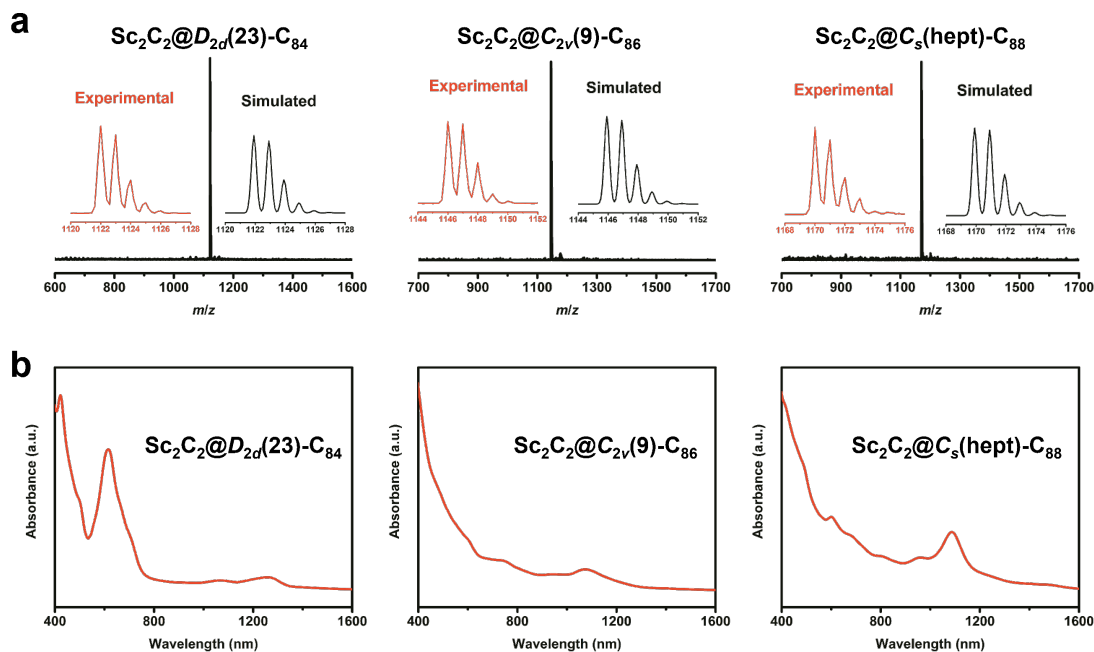




Supplementary Fig. 25 Schematic of the tip and sample geometry used to solve the 3D electromagnetic wave equation using FDTD numerical method. **a**, The model with the Au tip apex and the Au substrate surface. **b**, The model with two gold tip apex for both electrodes. (Left) The separation d between the two Au tips is set to 1 nm. COMSOL simulation showing the spatial distribution of the electric field decays with lateral spatial diffusion. (Right) Electric field decay curve along the red line in the left figure.

Here, we consider two junction geometries (**Supplementary Fig. 25**), one with Au tip apex and the Au substrate surface; the other with gold tip apex for both electrodes. The nanogap between the electrodes is set to 1 nm according to our single-metallofullerenes junction. When the voltage is applied between the electrodes, the electric field in the STM junction depends mainly on the spatial distribution. For example, in the Au tip apex and the Au substrate surface geometry, when the voltage 0.1 V is applied, the electric field can reach 3.8×10^8 V/m around the Au tip, and decay rapidly with lateral expansion (along the red line), and only 1×10^8 V/m at 5 nm. In the gold tip apex for both electrodes geometry, the situation is similar. When the voltage 0.1 V is applied, the electric field can reach 2.4×10^8 V/m around the Au tip and decay rapidly with lateral expansion (along the red line), and only 0.6×10^8 V/m at 5 nm. Hence, from the view of electric field decay, our metallofullerenes devices can operate independently without interfering with other devices

S8. Molecular preparation and chemical nomenclature



Supplementary Fig. 26 The physical properties of $\text{Sc}_2\text{C}_2@D_{2d}(23)\text{-C}_{84}$, $\text{Sc}_2\text{C}_2@C_{2v}(9)\text{-C}_{86}$, $\text{Sc}_2\text{C}_2@C_s(\text{hept})\text{-C}_{88}$. **a**, Mass spectra. **b**, Vis-NIR absorption spectra.

To establish the nomenclature for nonclassical heptagon-containing fullerenes is still underway, though theoretical investigation on such nonclassical fullerenes has been for more than thirty years. Some software such as the revised version of CaGe and the GSW (Generalized Stone-Wales) programs have been proposed for systematic searching nonclassical structures, but this software for nonclassical cages is still saved by individuals and groups. The reasons for this dilemma starkly different from the nomenclature of spiral code for classical fullerenes with hexagons and pentagons⁹ might be as follows:

Firstly, the amount of heptagon-containing fullerenes is much larger than classical isomers. For example, the isomer numbers of nonclassical fullerenes with pentagons, hexagons, and one heptagon are 2784 for C_{50} , 36294 for C_{60} , and 289705 for C_{70} . If more heptagons were included, the isomers would be much more. Secondly, the experimentally identified heptagon-containing fullerenes are limited in single-digit, especially for those with two or more heptagons¹⁰⁻¹² [Note that Su-Yuan Xie, one of our corresponding co-authors, is also a pioneer to synthesize nonclassical fullerenes with 1-2 heptagon(s)]. Moreover, a classical fullerene in the experiment can use its spiral enumeration to find a corresponding spiral number while the spiral enumeration is inapplicable for nonclassical isomers. Huge amounts of isomers are needed to compare with the experiment structure for its serial number, which is arduous especially for large fullerenes like C_{88} . Therefore, given that universal nomenclature for heptagon-containing fullerenes is still absent and only a very few isomers of nonclassical fullerene can be synthesized in experiments, experimenters usually define hept C_{2n} or $\text{C}_{2n}(\text{hept})$

plus symmetry for an individual structure of nonclassical fullerene-like the case of Cs(hept)-C₈₈ reported in this manuscript.

- 1 Yang, Q. *et al.* Design of Single-Molecule Multiferroics for Efficient Ultrahigh-Density Nonvolatile Memories. *Adv Sci (Weinh)* **6**, 1801572 (2019).
- 2 Li, J. J. *et al.* Giant single-molecule anisotropic magnetoresistance at room temperature. *J. Am. Chem. Soc.* **137**, 5923-5929 (2015).
- 3 Miyamachi, T. *et al.* Robust spin crossover and memristance across a single molecule. *Nat. Commun.* **3**, 938 (2012).
- 4 Kao, K. C. Dielectric phenomena in solids with emphasis on physical concepts of electronic processes Ch. 2 (Elsevier Academic Press, 2004)
- 5 Vrouwe, S. A. G. *et al.* Mechanics of lithographically defined break junctions. *Phys. Rev. B* **71**, 035313 (2005).
- 6 Reed, M. A., Zhou, C., Muller, C. J., Burgin, T. P. & Tour, J. M. Conductance of a Molecular Junction. *Science* **278**, 252-254 (1997).
- 7 Liu, J. *et al.* Transition from Tunneling Leakage Current to Molecular Tunneling in Single-Molecule Junctions. *Chem* **5**, 390-401 (2019).
- 8 Linn, E., Rosezin, R., Tappertzhofen, S., Bottger, U. & Waser, R. Beyond von Neumann--logic operations in passive crossbar arrays alongside memory operations. *Nanotechnology* **23**, 305205, (2012).
- 9 Nakanishi, R. *et al.* DySc₂N@C₈₀ Single-Molecule Magnetic Metallofullerene Encapsulated in a Single-Walled Carbon Nanotube. *J. Am. Chem. Soc.* **140**, 10955-10959 (2018).
- 10 Tian, H.-R. *et al.* An Unconventional Hydrofullerene C₆₆H₄ with Symmetric Heptagons Retrieved in Low-Pressure Combustion. *J. Am. Chem. Soc.* **141**, 6651-6657 (2019).
- 11 Zhong, Y.-Y. *et al.* Double Negatively Curved C₇₀ Growth through a Heptagon-Involving Pathway. *Angew. Chem. Int. Ed.* **58**, 14095-14099 (2019).
- 12 Tan, Y.-Z. *et al.* Carbon arc production of heptagon-containing fullerene[68]. *Nat. Commun.* **2**, 420, (2011).